ACSNANO

www.acsnano.org

ARTICLE

A Two-Pronged Nanostrategy of Iron Metabolism Disruption to Synergize Tumor Therapy by Triggering the Paraptosis–Apoptosis Hybrid Pathway

Huali Lei, Guanghui Hou,* Lin Liu, Zifan Pei, Youdong Chen, Yujie Lu, Nalin Yang, Shumin Sun, and Liang Cheng*

Cite This: https://doi.org/10.1021/acsnano.4c06199

Read Online

ACCESS | Metrics & More | Article Recommendations | Supporting Information

ABSTRACT: Iron metabolism has emerged as a promising target for cancer therapy; however, the innate metabolic compensatory capacity of cancer cells significantly limits the effectiveness of iron metabolism therapy. Herein, bioactive gallium sulfide nanodots (GaS_x), with dual functions of "reprogramming" and "interfering" iron metabolic pathways, were successfully developed for tumor iron metabolism therapy. The constructed GaS_x nanodots ingeniously harness hydrogen sulfide (H_2S) gas, which is released in response to the tumor microenvironment, to reprogram the inherent transferrin receptor 1 (TfR1)-ferroportin 1 (FPN1) iron metabolism axis in cancer cells. Concurrently, the gallium ions (Ga^{3+}) derived from GaS_x act as a biochemical "Trojan horse", mimicking the role of iron and displacing it from essential biomolecular binding sites, thereby influencing the fate of cancer cells. By leveraging the dual mechanisms of Ga^{3+}-mediated iron disruption and H_2S-facilitated reprogramming of iron metabolic pathways, GaS_x prompted the initiation of a paraptosis–apoptosis hybrid pathway in cancer cells, leading to marked suppression of tumor proliferation. Importantly, the dysregulation of iron metabolism induced by GaS_x notably increased tumor cell susceptibility to both chemotherapy and immune checkpoint blockade (ICB) therapy. This study underscores the therapeutic promise of gas-based interventions and metal ion interference strategies for the tumor metabolism treatment.

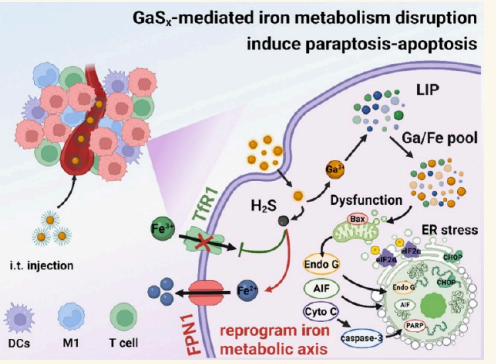

KEYWORDS: *Bioactive nanomaterials, iron metabolism, paraptosis, gas therapy, synergistic cancer therapy*

1. INTRODUCTION

Metabolic reprogramming is a key hallmark of cancer and is characterized by altered metabolic pathways for nutrients such as glucose, amino acids, and fatty acids.[1,2] Targeting these metabolic pathways offers a promising strategy for impeding tumor progression. However, the effectiveness of current metabolic therapy is hindered by the intricate and adaptable tumor metabolic networks.[3−5] This underscores the need for more effective metabolic strategies. Micronutrient metal ions are pivotal for tumor growth and differentiation, where they serve essential roles in complex physiological and biochemical processes, including energy conversion, signal transduction, and metabolic regulation.[6] Consequently, manipulating the availability of nutrient metal ions poses a potential strategy for cancer metabolic therapy.

Iron (Fe), a vital nutrient metal ion, is indispensable for cellular growth and metabolism. It plays an important role in key biological processes, such as oxygen transport, redox reactions, and DNA synthesis.[7,8] The pronounced need for Fe in rapidly proliferating tumor cells, a phenomenon known as "iron addiction", makes iron metabolism a target for cancer therapy. Current strategies for disrupting iron metabolism in cancer therapy focus on two main approaches: one that inhibits Fe efflux, termed "iron increase therapy," and another that depletes Fe stores, known as "iron removal therapy".[9−12] For example, the inhibition of ferroportin 1 (FPN1) effectively reduces intracellular Fe efflux, causing Fe accumulation and

Received: May 10, 2024
Revised: July 28, 2024
Accepted: July 30, 2024

Scheme 1. Two-Pronged Iron Metabolism Disruption Strategy Potentiates Tumor Therapy by Triggering the Paraptosis−Apoptosis Hybrid Pathway: (a) Synthesis and Modification of GaS_x; (b) GaS_x-Mediated Iron Metabolism Disruption Induces Tumor Paraptosis−Apoptosis; (c) GaS_x Overcomes Chemotherapy Resistance by Disrupting Iron Metabolism; (d) GaS_x-Induced Paraptosis in Tumor Cells To Activate the Immune Response

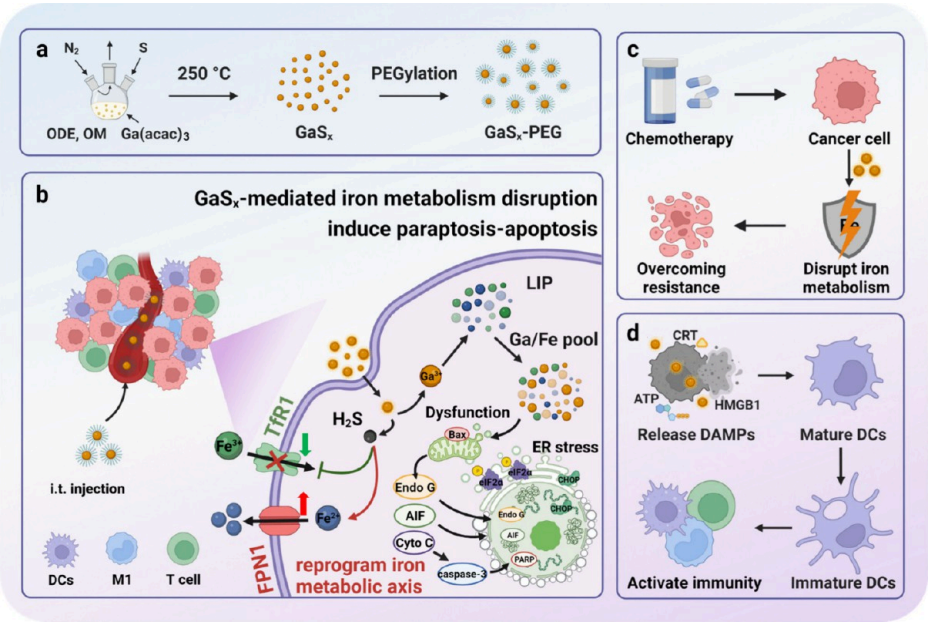

subsequent induction of ferroptosis in cancer cells.[13,14] Additionally, Fe chelators, such as deferoxamine (DFO), deferiprone, and deferasirox have been utilized to actively eliminate Fe from cells, triggering Fe-related dysfunction and apoptosis.[15,16] Nevertheless, these treatments do not fully address the compensatory mechanisms of tumor iron metabolism. Cancer cells can maintain intracellular iron homeostasis by actively regulating the transferrin receptor 1 (TfR1)-FPN1 iron metabolic axis, leading to suboptimal efficacy of iron metabolism therapy.[17] Therefore, more approaches are urgently needed to effectively target tumor iron metabolism.

A promising method involves directly blocking the scarce Fe ion sites in cancer cells to initiate "iron interference", which can circumvent compensatory iron metabolic pathways in tumors and achieve more effective iron metabolism-targeted therapy. Given that gallium ions (Ga^{3+}) shares analogous properties with Fe^{3+}, including ionic radius, electron affinity, and electronegativity, cells generally cannot distinguish accurately between them.[18,19] Nonetheless, Ga^{3+} cannot functionally substitute Fe^{3+} in cells since it lacks the ability to undergo reduction. Therefore, Ga^{3+} can operate as a "Trojan horse" by mimicking Fe^{3+}, causing iron dysfunction. Exploiting this, Ga-based pharmaceuticals such as gallium nitrate ($Ga(NO_3)_3$) have been approved for clinical use against antibacterial and hypercalcemic deseaes.[20,21] However, the research into exploiting Ga for the disruption of iron metabolism in tumor therapy remains nascent. Thus, probing into methodologies leveraging Ga to disrupt tumor iron metabolism is imperative for tumor iron metabolism treatment.

On the other hand, the effectiveness of gallium-mediated "iron interference" substantially depends on competitive interactions within the abundant labile iron pool (LIP) in tumor cells.[22] To enhance the efficacy of gallium-mediated "iron interference", it is suggested that prompting cancer cells to actively purge their internal LIP could be beneficial.[23,24] Hydrogen sulfide (H_2S), a gaseous signaling molecule, affects multiple physiological processes, including mitochondrial function and energy generation. However, the potential regulatory impact of H_2S on tumor iron metabolism remains underexplored.[25,26] Given the profound association between H_2S and pivotal signaling molecules like hypoxia-inducible factor 1 (HIF-1) and hepcidin that regulate iron metabolism, H_2S has great potential to regulate iron metabolism in tumor cells and augment the "iron interference" effect of Ga^{3+}.[27]

Herein, we demonstrated the potent capacity of H_2S gas to reshape the iron metabolic axis in cancer cells. The integration of H_2S and Ga^{3+} is expected to achieve efficient tumor therapy through the targeting of iron metabolism (Scheme 1). The bioactive GaS_x nanodots were synthesized and examined for their potential as iron metabolism disruptors. GaS_x released Ga^{3+} and H_2S in response to the tumor environment, and the released H_2S gas reshaped the TfR1-FPN1 iron metabolism axis, thereby amplifying the iron interference effect of Ga^{3+}. GaS_x-induced iron metabolism disruption led to mitochondrial dysfunction in cancer cells, triggering the release of mitochondria-associated pro-apoptotic factors such as cytochrome c (Cyt C), apoptosis-inducing factor (AIF), and endonuclease G (Endo G). This process simultaneously activated both caspase-3-dependent and caspase-3-independent apoptotic pathways. Importantly, GaS_x-mediated iron metabolism disruption also triggered endoplasmic reticulum (ER) stress, ultimately leading to tumor cell paraptosis. Leveraging its capacity to induce multiple modes of cell death by disrupting iron metabolism, GaS_x demonstrated significant tumor growth inhibition. Furthermore, the modulation of iron metabolism-related cascades by GaS_x notably sensitized tumors to the effects of chemotherapy and PD-1 immune checkpoint blockade (ICB) therapy. Our study demonstrates the potential of an ion interference strategy in tumor metabolism treatment, and provides an idea for the potentiation of existing clinical treatments.

https://doi.org/10.1021/acsnano.4c06199
ACS Nano XXXX, XXX, XXX−XXX

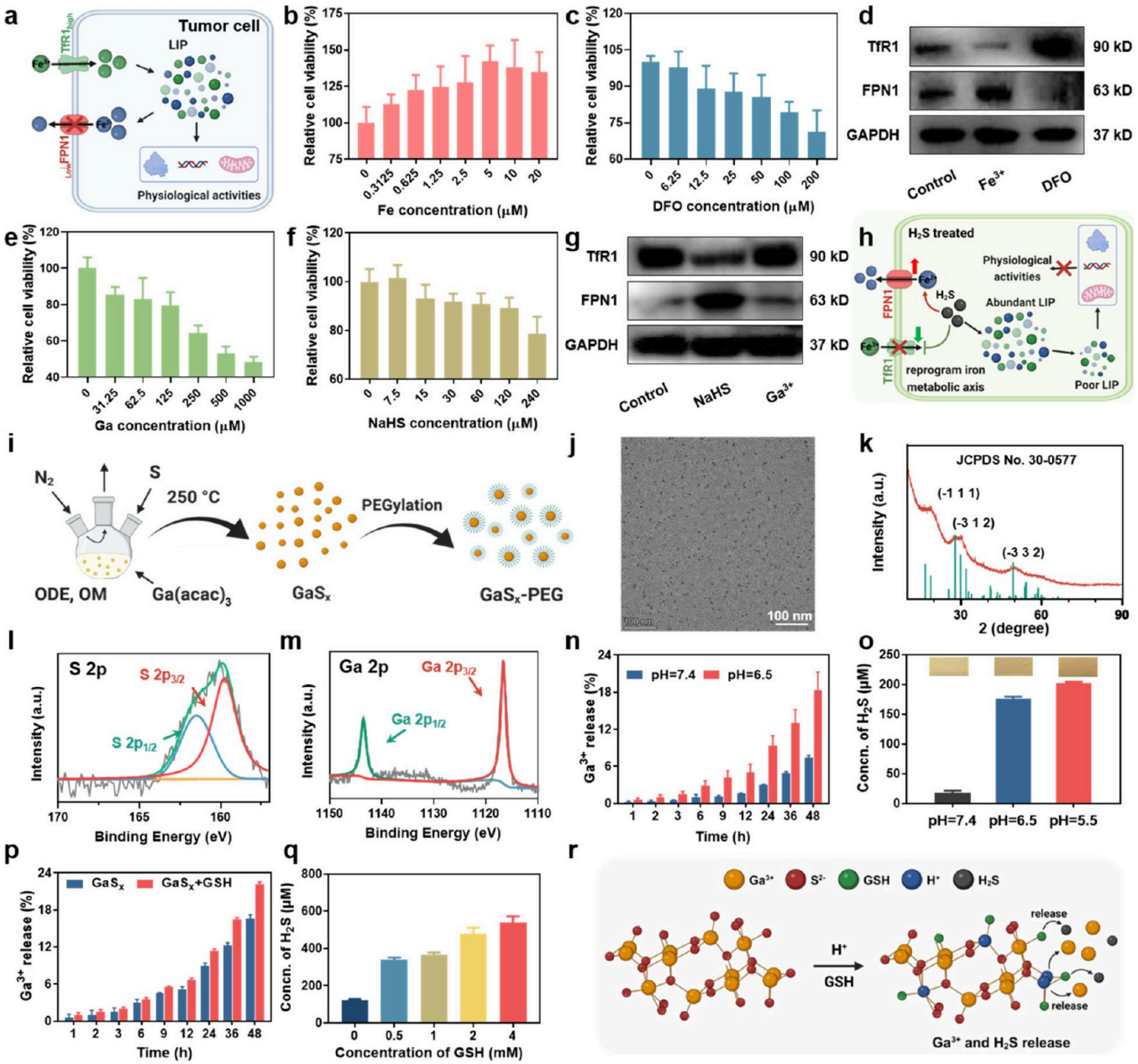

Figure 1. Iron metabolism investigation and GaS_x nanodots synthesis. (a) Scheme of iron metabolism in healthy tumor cells. (b) Relative cell viability of CT26 cells after incubation with Fe^{3+} solutions (the medium without FBS) for 12 h. (c) Relative cell viability of CT26 cells after incubation with DFO for 12 h. (d) WB detection of iron metabolism regulatory axis-related proteins, including TfR1 and FPN1, in CT26 cells after treatment with Fe^{3+} solutions and DFO. (e) Relative cell viability of CT26 cells after incubation with Ga^{3+} solutions for 12 h. (f) Relative cell viability of CT26 cells after incubation with NaHS for 12 h. (g) WB detection of iron metabolism regulatory axis-related proteins, including TfR1 and FPN1, in CT26 cells after incubation with NaHS and Ga^{3+} solution. (h) Scheme of H_2S-mediated disruption of iron metabolism in tumor cells. (i) Scheme of GaS_x synthesis and modification. (j) Transmission electron microscopy (TEM) image of GaS_x. (k) X-ray diffraction (XRD) analysis of GaS_x. (l) X-ray photoelectron spectroscopy (XPS) of the S 2p region in GaS_x. (m) XPS spectrum of the Ga 2p region in GaS_x. (n) Ga^{3+} release from GaS_x in different pH buffers. (o) H_2S release from GaS_x in different pH buffers. (p) Ga^{3+} release from GaS_x in solutions containing different concentrations of GSH. (q) H_2S release from GaS_x in solutions containing different concentrations of GSH. (r) Scheme of H_2S and Ga^{3+} release from GaS_x.

2. RESULTS AND DISCUSSION

2.1. Exploration of the Ga^{3+}'s Ability to Disrupt Iron Metabolism. Due to the rapid proliferation of malignant tumors and increased synthetic and metabolic activity, the tumor cells exhibit heightened demand for Fe ions (Figure 1a). The importance of Fe was substantiated by incubating CT26 cells with varying concentrations of $FeCl_3$ in cell culture medium devoid of fetal bovine serum (FBS). It was observed that cell viability relative to the control was increased in a concentration-dependent manner at Fe^{3+} concentrations below 5 μM, indicating that Fe^{3+} effectively stimulated tumor cell proliferation (Figure 1b). Conversely, treatment with the iron chelator DFO significantly decreased the viabilities of CT26 cells, highlighting the crucial role of Fe^{3+} in sustaining tumor cell proliferation (Figure 1c). These findings suggested that iron metabolism was a potential target in tumor therapy.

https://doi.org/10.1021/acsnano.4c06199
ACS Nano XXXX, XXX, XXX−XXX

Notably, tumor cells are capable of sensing their own iron content and tightly regulating iron levels through iron metabolic compensatory mechanisms. When exposed to surplus Fe^{3+}, iron-overloaded CT26 cells reduced iron intake by downregulating TfR1 and enhanced iron efflux by upregulating FPN1 (Figure 1d). Conversely, DFO-induced Fe^{3+} removal led to an increase in TfR1 and a decrease in FPN1, signaling enhanced iron uptake of the cells. This strongly supported the notion that cancer cells maintain iron homeostasis by modulating the TfR1-FPN1 axis, which was a notable challenge to the current strategies targeting iron metabolism. Interestingly, due to its iron-mimicking properties, Ga^{3+} offers a promising means of disrupting iron function and inhibiting cellular proliferation. Following treatment with the FDA-approved gallium compound $Ga(NO_3)_3$, the cell viabilities significantly decreased, validating the capability of Ga^{3+} to suppress tumor cell growth (Figure 1e). Importantly, $Ga(NO_3)_3$ treatment had a minimal impact on the expression levels of TfR1 and FPN1. This finding implied that Ga^{3+} could disrupt iron metabolism without triggering cancer cell iron compensation responses, thereby revealing the distinctive benefit of targeting iron metabolism with Ga^{3+}. A noteworthy factor was made concerning the high levels of LIP in cancer cells, a competitive factor against Ga^{3+} for iron-binding sites in cancer cells, implying that elevated Ga^{3+} concentrations might be necessary to effectively target cancer cells, yet raising potential safety concerns (Figure 1e). Tumor cells with a penchant for iron typically ramp up TfR1 expression while downplaying FPN1 to bolster iron absorption and curtail its efflux, thus maintaining a heightened LIP.[28] Hence, reprogramming the $TfR1_{(high)}$-$FPN1_{(low)}$ metabolic axis in cancer cells to the iron efflux mode ($TfR1_{(low)}$-$FPN1_{(high)}$) not only directly influences iron metabolism but also holds great potential for significantly improving the iron interference effect of Ga^{3+}. Notably, treatment with the H_2S donor NaHS substantially decreased TfR1 expression while increasing FPN1 expression in CT26 cells (Figure 1g). Meanwhile, due to the potential reprogramming function of H_2S on the iron metabolism axis in tumor cells, H_2S had been demonstrated the ability to inhibit tumor cell growth (Figure 1f). These findings confirmed that the gaseous signaling molecule H_2S could reprogram the iron metabolic pathway in tumor cells (Figure 1h), a process likely interconnected with the substantial role of H_2S in modulating key regulators of iron metabolism, such as hepcidin and HIF-1.[29] Consequently, the strategic combination of Ga^{3+} with H_2S hold great promise for the development of interventions that effectively disrupted iron metabolism in tumors.

2.2. GaS_x Nanodots Synthesis and Characterization. To integrate the iron interference ability of Ga^{3+} and the potential of H_2S to reprogram the iron metabolism system, the bioactive GaS_x nanodots were synthesized using a high-temperature thermal decomposition method. These nanodots are designed to deliver both Ga^{3+} and H_2S concurrently for iron metabolism therapy (Figure 1i). Transmission electron microscopy (TEM) image revealed the ultrasmall morphology of the GaS_x nanodots in the oil phase with a size of ~8 nm (Figure 1j). Additionally, a strong colocalization of Ga and S was observed via EDS elemental mapping (Supporting Figure S1). X-ray diffraction (XRD) analysis indicated that the diffraction peaks of GaS_x in the oil phase matched well with those of Ga_2S_3 (JCPDS No. 30-0577, Figure 1k). Furthermore, the valence states of Ga and S in GaS_x in the oil phase were detected by X-ray photoelectron spectroscopy (XPS). The full-scan XPS spectra showed characteristic peaks of Ga and S (Supporting Figure S2). Notably, in the S 2p region, the binding energies (BE) appeared at ~159.78 eV and ~161.48 eV for S $2p_{3/2}$ and S $2p_{1/2}$, respectively, consistent with the −2 valence of S and necessary for H_2S generation (Figure 1l). In the Ga 2p region, the BEs for Ga $2p_{3/2}$ and Ga $2p_{1/2}$ were approximately 1118.78 and 1143.48 eV, respectively, which were indicative of the valence state of +3 for Ga (Figure 1m). This similarity to the valence of Fe^{3+} is critical for disrupting iron metabolism in tumor cells. Furthermore, ultrasmall GaS_x exhibited identical fluorescence, which was similar to that of Ga_2S_3 quantum dots, providing further verification of the successful synthesis of GaS_x (Supporting Figures S3 and S4).[30] DSPE-PEG_{5k} is an amphiphilic macromolecule that is a conjugated compound of phosphatidyl bipyramid and polyethylene glycol, where the phosphatidyl bipyramid portion is lipophilic and able to react with the oleylamine and oleic acid on the surface of gallium sulfide nanodots, while the polyethylene glycol part is hydrophilic. Therefore, to enhance the solubility and biocompatibility of GaS_x in biological environments, the synthesized nanodots were modified with DSPE-PEG_{5K}. Dynamic light scattering (DLS) showed that the hydrated particle size of the PEGylated GaS_x was ~13 nm (Supporting Figure S5). GaS_x dispersions remained stable in the physiological solutions at room temperature for 7 days, including water, saline, phosphate-buffered saline (PBS), and RPMI medium, without any visible precipitates (Supporting Figure S6a). While slight decreases were noted in both UV−vis-NIR absorption and hydrated particle size, over 75% of GaS_x remained, suggesting not only high physiological stability but also potential for biodecomposition (Supporting Figure S6b and S6c). Subsequently, the biological activity of GaS_x was confirmed by detecting the release of H_2S and Ga^{3+}. Ga^{3+} was gradually released from GaS_x over time, and approxiamtely 7.5% of Ga^{3+} was effectively released after 48 h, which confirmed the successful decomposition of GaS_x (Figure 1n). Additionally, the GaS_x suspension not only induced pronounced darkening of the lead acetate test paper but also promoted interaction with methylene blue (MB) to yield methylene blue sulfide, as evidenced by the distinct absorption peak at 668 nm. 35.4 μM of H_2S was released when the concentration of GaS_x reached to ~50 ppm, which further confirmed the ability of GaS_x to decompose and release H_2S (Supporting Figures S7 and S8). All these results collectively affirmed the biological activity of GaS_x, which was essential to ensure sustainable supplies of Ga^{3+} and H_2S.

Considering the acid sensitivity and reduction sensitivity of metal sulfides, it is anticipated that weak acid and a reducing tumor microenvironment could accelerate the decomposition rate of GaS_x. When dispersed in a weakly acidic buffer solution, GaS_x exhibited a noticeable fading in color, a marked decrease in UV−vis-NIR absorption, and a reduction in particle size. And the release rate of Ga^{3+} was increased to ~18.4% after 48 h (Supporting Figure S9). This acid-catalyzed degradation could stem from the interaction of protons with sulfide ions (S^{2-}) in GaS_x, yielding H_2S gas. The pH-dependent release of H_2S from GaS_x was confirmed by using lead acetate paper and the Washington State Prop-1 (WSP-1) fluorescent probe. The release of H_2S in buffer at pH 7.4 was 18.2 μM, while at pH 6.5 and pH 5.5, the release of H_2S increased to 175.9 and 201.6 μM, respectively. (Figure 1o). Additionally, the presence of GSH substantially increased the release rate of Ga^{3+} and H_2S from GaS_x as compared to standard condition. After

https://doi.org/10.1021/acsnano.4c06199
ACS Nano XXXX, XXX, XXX−XXX

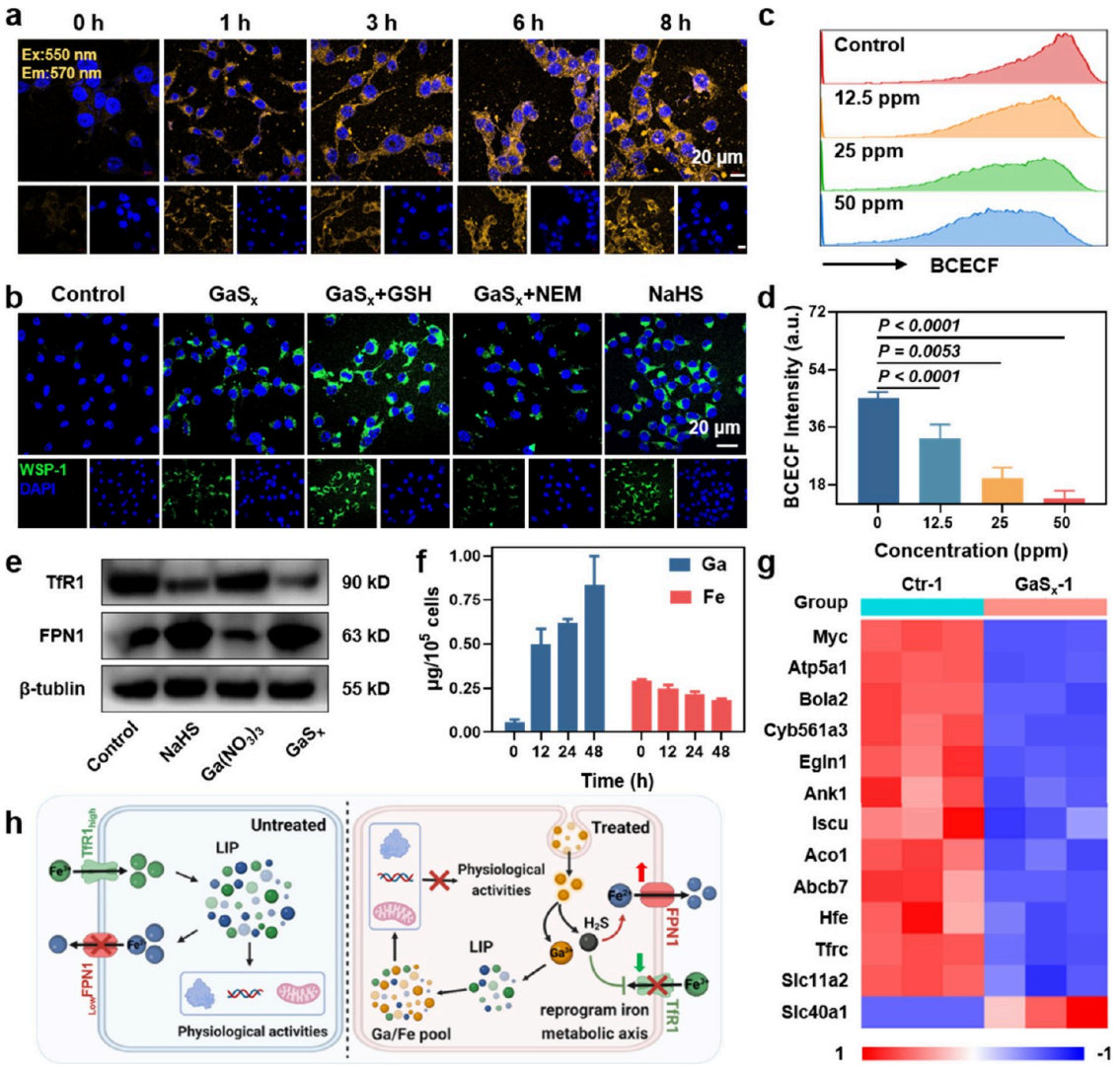

Figure 2. GaS_x disrupted tumor cell iron metabolism. (a) Confocal images of CT26 cell endocytosis after GaS_x incubation for different time. (b) Confocal images of WSP-1 fluorescence staining of CT26 cells after different treatments. (c) BECEF signaling detection in CT26 cells by flow cytometry after treatment with different concentrations of GaS_x. (d) Statistical analysis of the BECEF signals in each group in (b). (e) WB detection of iron metabolism regulatory axis-related proteins, including TfR1 and FPN1, in CT26 cells after different treatments. (f) Determination of Ga and Fe contents in CT26 cells after GaS_x treatment for different time by ICP-MS. (g) Clustering heat map of differential genes related to iron metabolism. (h) Scheme of the mechanism by which GaS_x disrupted iron metabolism in tumor cells.

incubation with the GSH solution, the percentage of released Ga^{3+} increased from 16.5% to 22.2%, while the release of H_2S was also enhanced from ~121.1 to ~537.2 μM (Figure 1p and 1q, and Supporting Figure S10). This GSH-promoted disassembly of GaS_x was attributed to the thiol groups in GSH replacing the sulfide sites in GaS_x (Figure 1r). These data confirmed that GaS_x effectively released Ga^{3+} and H_2S in response to the tumor microenvironment, which was essential for GaS_x to accurately target and disrupt iron metabolism within tumors. Additionally, the biocompatibility of GaS_x was assessed by hemolysis experiment. No obvious hemolysis phenomenon was detected even at high concentrations of GaS_x up to 640 ppm, highlighting its exceptional biosafety profile for further biological testing (Supporting Figure S11). In short, we successfully synthesized bioactive GaS_x nanodots. GaS_x exhibits robust ability to release Ga^{3+} and H_2S in response to acidic and reductive condition of the tumor microenvironment. This responsiveness makes GaS_x a promising candidate for precise and targeted interventions in cancer treatment.

2.3. GaS_x Regulated Cellular Iron Metabolism and Induced Apoptosis. Effective cellular uptake is a key prerequisite for the biological effects of GaS_x. The cellular uptake ability of GaS_x was verified by utilizing its inherent fluorescence properties. As the incubation time increased, the fluorescence signal of GaS_x in the cells notably enhanced, indicating the time-dependent cellular uptake of GaS_x nanodots (Figure 2a and Supporting Figure S12). The influence of GaS_x on iron metabolism heavily relies on its decomposition products, Ga^{3+} and H_2S. To track H_2S release within cells by GaS_x, a WSP-1 fluorescent probe was employed. A distinct green fluorescent signal was detected in cells treated with GaS_x nanodots, signifying the effective intracellular release of H_2S upon GaS_x internalization. Furthermore, the intensity of the green fluorescent signals substantially increased with the addition of GSH, however diminished upon the addition of NEM (a thiol-binding agent with GSH neutralizing capability), indicating the role of GSH in promoting GaS_x decomposition and enhancing H_2S release (Figure 2b and Supporting Figure

https://doi.org/10.1021/acsnano.4c06199
ACS Nano XXXX, XXX, XXX−XXX

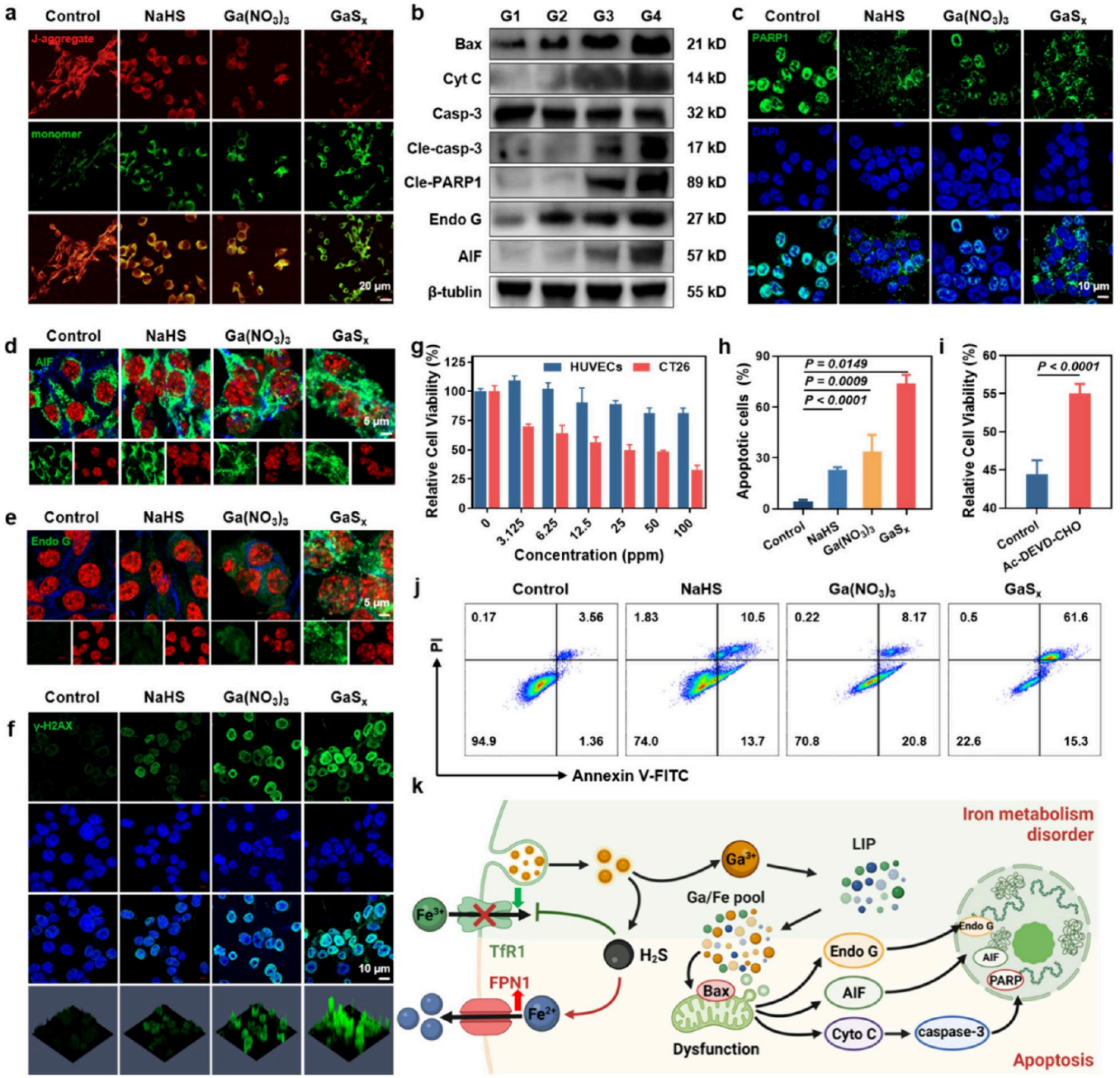

Figure 3. GaS_x induced apoptosis in tumor cells. (a) Confocal images of JC-1 fluorescence staining of CT26 cells after different treatments. (b) WB detection of apoptosis-related proteins, including Bax, Cyt C, cleaved-caspase-3, cleaved-PARP1, Endo G, and AIF, in CT26 cells after different treatments (G1: Control, G2: NaHS, G3: $Ga(NO_3)_3$, and G4: GaS_x). (c) Confocal images of PARP1 fluorescence staining of CT26 cells after different treatments. (d) Confocal images of AIF fluorescence staining of CT26 cells after different treatments. (e) Confocal Endo G images of fluorescence staining of CT26 cells after different treatments. (f) Confocal images of γ-H2AX fluorescence staining of CT26 cells after different treatments. (g) Killing effects of GaS_x at different concentrations on HUVECs and CT26 cells. (h) Proportion of apoptotic cells after different treatments in (j). (i) Cell killing effects of GaS_x before and after incubation with apoptosis inhibitors. (j) Flow cytometric analysis of CT26 cell apoptosis after different treatments. (k) Scheme of the mechanism of GaS_x killing tumor cells.

S13). H_2S has been shown to cause lactic acid accumulation and tumor acidification by regulating tumor cell glycolysis.[31] Thus, the pH fluctuations in CT26 cells post-GaS_x treatment were scrutinized using a fluorescent probe 2′,7′-bis(2-carboxyethyl)-5-(and-6)-carboxyfluorescein, acetoxymethyl ester (BCECF AM). The BCECF signal diminished as the concentration of GaS_x escalated, signifying the effective instigation of tumor cell acidification by GaS_x (Figure 2c and 2d). This further confirmed the capacities of GaS_x to supply H_2S and regulate cells. Due to the acid degradation behavior of GaS_x, H_2S-induced tumor acidification might initiate a positive feedback loop that promote GaS_x decomposition and iron interference. These findings affirmed the successful internalization and subsequent breakdown of GaS_x into its active constituents.

Next, the relationship between GaS_x treatment and iron metabolism was investigated by examining the TfR1-FPN1 metabolic axis, which was pivotal for cell iron homeostasis.

https://doi.org/10.1021/acsnano.4c06199
ACS Nano XXXX, XXX, XXX−XXX

Western blot assays of TfR1 and FPN1 in CT26 cells post-GaS_x treatment were performed, with NaHS (H_2S donor) and $Ga(NO_3)_3$ (clinical gallium drug) serving as comparatives. In comparison to the untreated control, treatment with $Ga(NO_3)_3$ had a negligible effect on the expression levels of TfR1 and FPN1 in cancer cells (Figure 2e). Notably, both NaHS and GaS_x treatments significantly reduced the expression of TfR1 and increased the expression of FPN1 in CT26 cells. These results suggested that GaS_x treatment successfully reprogrammed the iron metabolic axis in CT26 cells, probably due to the close correlation of H_2S with upstream signaling of the iron metabolic axis. To further confirm the effect of GaS_x on iron metabolism, transcriptome sequencing was performed on CT26 cells before and after GaS_x treatment (Figure 2g). The heatmap highlighted consistent gene expression changes associated with iron metabolism, in line with what has been observed in the GaS_x treatment. The notable changes included the down-regulation of the transferrin receptor gene (Tfrc) and the iron homeostasis regulator gene (Hfe), and the significant up-regulation of the iron-regulated transporter gene (Slc40a1), mirroring the findings of the Western blot analysis and offering compelling evidence that GaS_x critically reprogrammed iron metabolism (Figure 2g).

The reversion of the TfR1-FPN1 axis contributes to a decrement in Fe uptake by cancer cells but encourages Fe expulsion, thereby depleting intracellular Fe levels. To conclusively ascertain the impact of GaS_x on iron metabolism, inductively coupled plasma mass spectrometry (ICP-MS) analysis was employed to quantify the intracellular Fe content. After GaS_x treatment, a steady uptick in cellular Ga content accompanied by a corresponding decline in Fe content was observed over time (Figure 2f), indicating the effectiveness of GaS_x in downregulating intracellular Fe levels. This could mitigate the competition between LIP and Ga^{3+}, and enhance the effect of Ga^{3+} on "iron interference" (Figure 2h). Therefore, the bioactive GaS_x nanodots exhibited a significant potential for disrupting intracellular iron metabolism through the synergistic effect of Ga^{3+}-mediated "iron interference" and H_2S-facilitated reshaping of the iron metabolic axis.

Mitochondria, which are critically involved in cellular iron storage, are significantly influenced by abnormalities in iron metabolism, which can cascade into widespread mitochondrial distress and impede various cellular energy-related functions.[32−34] Ga^{3+}, with its knack for occupying iron binding sites in mitochondria by imitating Fe^{3+}, endows GaS_x with a profound capacity to inflict mitochondrial damage. To evaluate the effects of GaS_x on mitochondrial function, a JC-1 probe was utilized to detect the changes in mitochondrial membrane potential of cells after treatment with NaHS, $Ga(NO_3)_3$ and GaS_x. It was found the treatment with NaHS and $Ga(NO_3)_3$ resulted in a noticeable increase in green fluorescence, indicating a level of mitochondrial integrity compromise (Figure 3a). However, treatment with GaS_x caused a pronounced loss of red fluorescence and a markedly intensified green signal, clearly demonstrating severe mitochondrial malfunction. These findings demonstrated that GaS_x causes mitochondrial distress by interfering with iron metabolism. Mitochondrial distress, pivotal in facilitating and amplifying apoptotic signals, occurs at the nexus of apoptotic pathways, caspase cascades, and subsequent cell death processes. Mitochondrial distress usually catalyzes the activation of the pro-apoptotic protein Bax.[35] Due to the effective iron interference effect of Ga^{3+}, the treatments with $Ga(NO_3)_3$ and GaS_x prompted the upregulation of Bax (Figure 3b). The heightened expression of Bax promotes pore creation in the mitochondrial membrane, boosting its permeability, and ultimately leading to Cyt C release. Confirming the above expectations, the cells treated with GaS_x manifested the most pronounced Cyt C expression (Figure 3b). The efflux of Cyt C from mitochondria catalyzes the cascade that activates caspase-3, furthering the apoptotic sequence by cleaving specific substrates, such as poly ADP-ribose polymerase (PARP), a hallmark of apoptosis. This biochemical chain reaction was indeed evident in the GaS_x-treated CT26 cells, which exhibited increased levels of cleaved caspase-3 and cleaved PARP1 (Figure 3b). Intriguingly, an ectopic appearance of PARP1 was also noted in the cells after GaS_x treatment (Figure 3c). These findings strongly confirmed the ability of GaS_x to activate the caspase-3 dependent apoptotic pathway through targeted interference in iron metabolism.

Amidst the mitochondrial dysregulation induced by the GaS_x-distorted iron metabolism, the expression of the mitochondrial proteins Endo G and AIF experienced a marked upsurge within CT26 cells post GaS_x intervention (Figure 3b). These proteins, upon being liberated into the cytosol, were observed to undertake translocation to the nucleus (Figures 3d and 3e). This translocation signified that the GaS_x-mediated disruption of iron homeostasis not only instigated mitochondrial dysfunction, but also facilitated the migration of Endo G and AIF, thereby endowing them with the role of DNA endonucleases that trigger the condensation of chromatin and the subsequent fragmentation of DNA. This series of events precipitated the activation of a caspase-3-independent apoptotic pathway. The infliction of nuclear DNA damage is a pivotal phase that culminates in the apoptotic process, and serves as an integral marker for the apoptotic death of tumor cells. To determine the magnitude of nuclear DNA damage wrought by the various treatments, the cells were subjected to staining with a γ-H2AX fluorescent probe (Figure 3f and Supporting Figure S14). Notably, discernible green fluorescent signals were observed in the nuclei of cells treated with NaHS and $Ga(NO_3)_3$, respectively, implying that alterations in the cellular iron metabolic axis due to H_2S and the interference from $Ga(NO_3)_3$ contributed to a certain degree of DNA damage. The γ-H2AX signal was significantly intensified in cells that underwent GaS_x treatment, revealing extensive DNA double-strand breaks and comprehensive destruction, which supplied potent internal signals that amplified apoptotic processes.

Encouraged by its potent capacities to disrupt iron metabolism and activate apoptosis, the cell-killing effect of GaS_x was further investigated. GaS_x exhibited a concentration-dependent cytotoxic effect against tumor cells, with over 25% of cancer cells killed at a concentration of 25 ppm (Figure 3g). The toxicity of GaS_x toward nontumorous cells was considerably reduced, and the cell viability was maintained above 80%, even at concentration as high as 100 ppm. This specificity was attributed to the heightened iron demand of tumor cells relative to that of the normal cells. Additionally, the inherently increased levels of GSH and the acidic intracellular milieu in CT26 cells facilitated the release of bioactive H_2S and Ga^{3+} from GaS_x nanodots, thereby amplifying their ability to kill cells. The discriminatory cytotoxicity exhibited by GaS_x toward cancer cells over noncancerous cells greatly accentuated its potential as a therapeutic agent targeting iron metabolism. Furthermore, Annexin V-FITC apoptosis detec-

https://doi.org/10.1021/acsnano.4c06199
ACS Nano XXXX, XXX, XXX−XXX

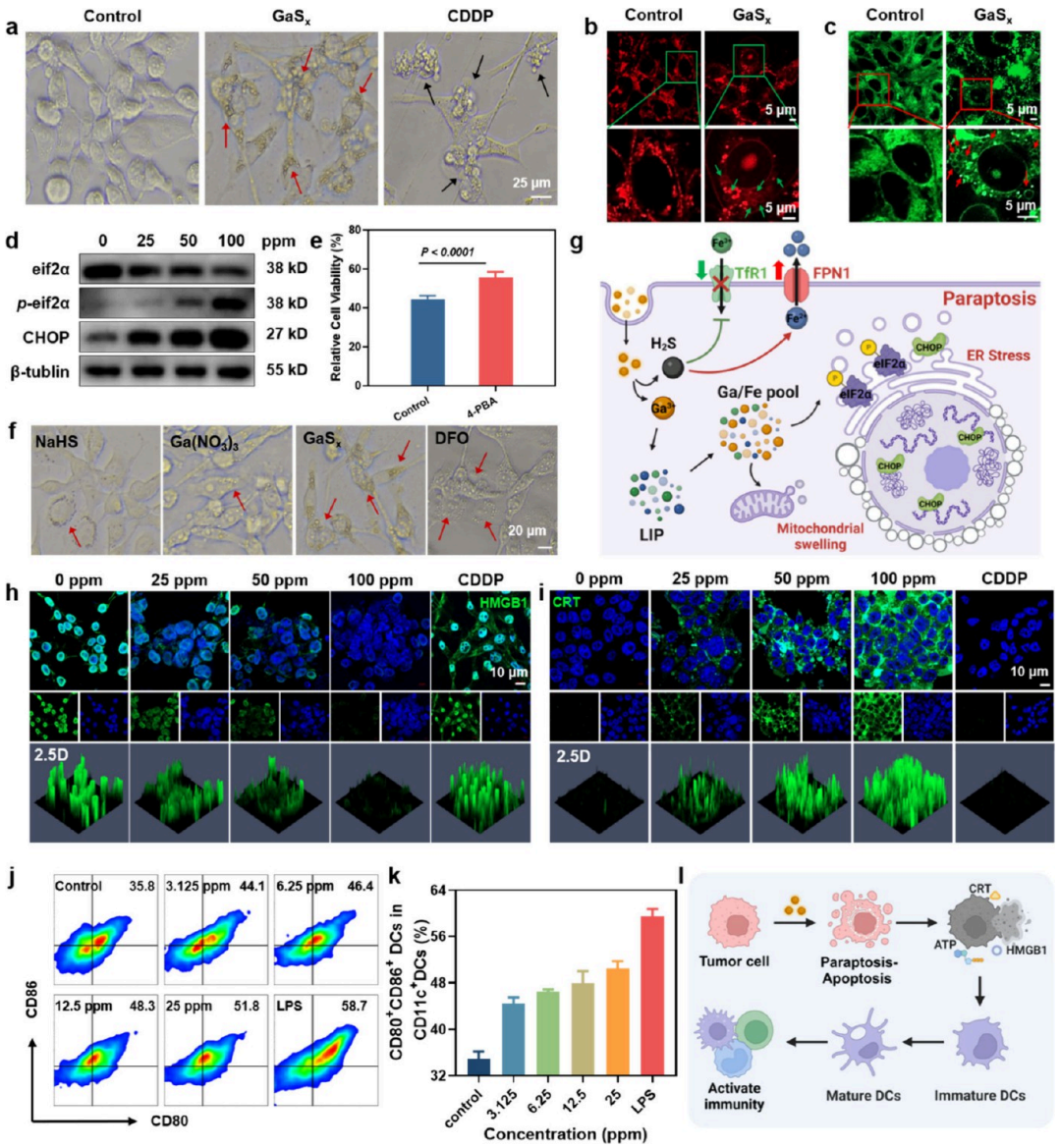

Figure 4. GaS_x induced paraptosis in tumor cells. (a) Photographs of paraptosis in CT26 cells after treatment with GaS_x and CDDP for paraptosis (Red arrows: paraptotic vesicles. Black arrows: apoptotic vesicles). (b) Confocal images of mitochondria stained with a fluorescent probe before and after GaS_x treatment (red: mitochondria). (c) Confocal images of fluorescent probe staining of ER before and after GaS_x treatment (green: ER). (d) WB detection of ER stress-related proteins, including *p*-eif2*α* and CHOP in CT26 cells after different treatments. (e) Relative cell viability of CT26 cells before and after treatment with the ER stress inhibitor (4-PBA). (f) Photographs of CT26 cells after various treatments (Red arrows: paraptotic vesicles). (g) Scheme of the mechanism of GaS_x-induced paraptosis in tumor cells. (h) Confocal images of HMGB1 levels in CT26 cells after treatment with different concentrations of GaS_x. Photographs of CT26 cell paraptosis after GaS_x and DFO treatment for 24 h. (i) Confocal images of CRT levels in CT26 cells treated with different concentrations of GaS_x. (j–k) Proportion of mature DCs after incubating DCs and supernatants from CT26 cells treated with different concentrations of GaS_x. (l) Scheme of GaS_x-induced paraptosis in tumor cells to activate the immune response.

tion kit revealed an augmented proportion of apoptotic cells after both NaHS and $Ga(NO_3)_3$ treatments (Figure 3h and 3j). Strikingly, GaS_x treatment led to an impressive 2.4-fold increase in the population of apoptotic cells compared to that in the control group, confirming the powerful induction apoptosis of GaS_x. Meanwhile, the application of the apoptosis inhibitor Ac-DEVD-CHO significantly reduced the cytotoxic potency of GaS_x, providing further support for the robust pro-apoptotic efficacy of GaS_x (Figure 3i). Above all, the tumor microenvironment-responsive release of H_2S and Ga^{3+} by GaS_x set the stage for a dual-pronged assault on cancer cells. H_2S reprogrammed the iron metabolic axis by suppressing TfR1 and augmenting FPN1 expression, which in turn diminished the intracellular LIP level via the curtailment of Fe^{3+} capture and the enhancement of Fe^{2+} expulsion (Figure 3k). Simultaneously, Ga^{3+} usurped the site of Fe^{3+} in crucial mitochondrial proteins, eliciting mitochondrial dysfunction. As a result, multiple pro-apoptotic factors, including Cyt C, EndoG, and AIF, were released from the mitochondria. These factors trigger the activation of both caspase-3 dependent and independent apoptotic pathways, leading to cell death.

2.4. GaS_x Induced Paraptosis in Tumor Cells. GaS_x has demonstrated potent efficacy in inducing apoptosis by disrupting iron metabolism. Notably, cancer cells usually

https://doi.org/10.1021/acsnano.4c06199
ACS Nano XXXX, XXX, XXX−XXX

deploy various mechanisms to evade apoptosis, such as overexpressing antiapoptotic proteins, suppressing pro-apoptotic factors, and triggering cell survival pathways. These survival tactics contribute to therapeutic resistance. Intriguingly, cancer cells resistant to one type of programmed cell death (PCD) might be more sensitive to other cell death modalities.[36] Therefore, simultaneous activation of multiple PCD pathways are considered to be a more effective tumor treatment strategy. Notably, the use of an apoptosis inhibitor only partially mitigated the cytotoxicity of GaS_x, indicating that GaS_x-induced cell death was not a singular type of apoptosis. To delve deeper into the cell death form induced by GaS_x, the GaS_x-induced cell death process was closely monitored. Interestingly, the cell death pattern induced by GaS_x significantly differed from apoptosis caused by cisplatin (CDDP), which is a well-established apoptotic agent. CDDP-treated cells displayed typical apoptotic features, such as cytoplasmic shrinkage, chromatin condensation, plasma membrane blebbing, and apoptotic body formation. However, CT26 cells exposed to GaS_x exhibited a different progression (Figure 4a). Although typical apoptotic bodies were observed in CT26 cells treated with GaS_x at the end of cell death, it was found that in the early stages of death, numerous vacuoles appeared around the nucleus, and the nucleus structure was remained intact (Figure 4a). This pattern more closely resembled the typical characteristic of paraptosis. Paraptosis is a type of nonapoptotic PCD that was documented in 2000 and remains underutilized in cancer therapy. Although its molecular mechanisms are not fully elucidated, the hallmarks of paraptosis, such as cytoplasmic vacuolation and swelling of the mitochondria and ER, have been well-defined.[37,38] To further validate the occurrence of paraptosis upon GaS_x treatment, the paraptosis-specific inhibitor cycloheximide (CHX) was introduced during the incubation of CT26 cells with GaS_x. A marked decrease in perinuclear vacuolation was observed, strongly confirming that GaS_x concurrently triggered paraptosis with apoptosis (Supporting Figure S15).

The occurrence of paraptosis is primarily attributed to the swelling of cell mitochondria and ER. To further validate the occurrence and potential mechanism of paraptosis, CT26 cells treated with GaS_x were stained with mitochondrial and ER tracking probes. The mitochondria in the control group exhibited a healthy filamentous morphology, whereas the mitochondria in the GaS_x-treated cells displayed distinct ring-shaped structure, suggesting that GaS_x induced mitochondrial swelling (Figure 4b). Previous studies have demonstrated that extreme conditions such as hypoxia or nutrient deficiency can significantly impact mitochondrial function, leading to the transformation of the filamentous structure of mitochondria to a swollen or ring-like state.[39,40] Given the critical role of iron in the mitochondrial function, particularly in hemoglobin synthesis and energy metabolism processes, it is likely that the mitochondrial swelling induced by GaS_x is a consequence of severe disturbance of iron homeostasis in cancer cells. Moreover, GaS_x-treated CT26 cells exhibited substantial changes in ER structure, with significant swelling and the formation of large vacuoles (Figure 4c), which corresponded to the observed cellular cavitation. ER swelling is a hallmark of ER stress. WB assay revealed that the expression of the ER stress-related proteins CHOP and *p*-elf2α was significantly increased in the GaS_x-treated cells in a concentration-dependent manner, indicating successful ER stress induction by GaS_x (Figure 4d). ER stress is considered as another major causative factor for paraptosis. The introduction of an ER stress inhibitor (4-phenylbutyric acid) significantly reduced the cytotoxic effects of GaS_x, highlighting the pivotal role of GaS_x-induced ER stress in tumor cell lethality (Figure 4e). The ER is also a crucial organelle in the cell that is responsible for protein synthesis and processing. The complex process of protein folding within the ER is dependent on multiple factors, such as ATP, chaperone proteins, glycosylases, elevated calcium levels, and oxidative conditions.[41] Consequently, protein folding within the ER is particularly vulnerable to disturbance in the cellular environment. GaS_x disrupted iron metabolism in cells, which inhibited energy generation and compromised protein function in cancer cells. These disruptions acted as stressors that interfere with protein folding processes in the ER, precipitating ER stress, and ultimately leading to the initiation of paraptosis.

To further confirm the correlation between GaS_x-induced paraptosis and iron metabolism disorder, the cells were further treated with NaHS, $Ga(NO_3)_3$, and the conventional iron chelator DFO. While NaHS and $Ga(NO_3)_3$ had less impact on iron metabolism than GaS_x, the presence of paraptotic vesicles was still detected following their administration (Figure 4f). Interestingly, DFO treatment resulted in a pronounced accumulation of paraptotic vacuoles, similar to that was observed in the GaS_x treatment (Figure 4f). These finding confirmed the association between GaS_x-mediated paraptosis and iron metabolism interference (Figure 4g). The consistency of GaS_x-induced vacuolation around the nucleus across various cell lines further validated the efficacy of GaS_x in triggering paraptosis across numerous tumor types (Supporting Figure S16).

The incidence of paraptosis is strongly dependent on ER stress, which triggers the movement of calreticulin (CRT) from the ER lumen to the cell surface while facilitating the release of the nuclear protein high mobility group box 1 (HMGB1).[42] Like damage-associated molecular patterns (DAMPs), these proteins act as hazard signals that initiate inflammatory reactions and orchestrate the activation of an immune response. Due to the effective induction of paraptosis, GaS_x was anticipated to expedite the release of DAMPs, thereby stimulating an immune response. The potential of GaS_x to activate the immune response was confirmed by detecting changes in the expression of DAMPs such as CRT and HMGB1 in CT26 cells after GaS_x treatment. The green fluorescence signal of HMGB1 in the nuclei showed a dose-dependent decrease in response to GaS_x treatment, indicating that GaS_x effectively induced the release of HMGB1 (Figure 4h and Supporting Figure S17). Meanwhile, the increase in the green fluorescence of CRT was dose-dependent after GaS_x treatment, indicating the translocation of CRT to the cell membrane (Figure 4i and Supporting Figure S18). These findings implied that GaS_x expedited the release of DAMPs, indicating that GaS_x potentiated immune responses. Notably, that the classical apoptosis induced by CDDP did not lead to substantial CRT exposure or HMGB1 release. This further underscored GaS_x's distinctive capacity to amplify the immune response by disrupting iron metabolism and inducing paraptosis.

These results indicated that GaS_x accelerated DAMPs release by disrupting iron metabolism and triggering paraptosis, suggesting its strong potential to activate the immune response. The released HMGB1 and exposed CRT act as "find me" and "eat me" signals, respectively, bolstering the

https://doi.org/10.1021/acsnano.4c06199
ACS Nano XXXX, XXX, XXX−XXX

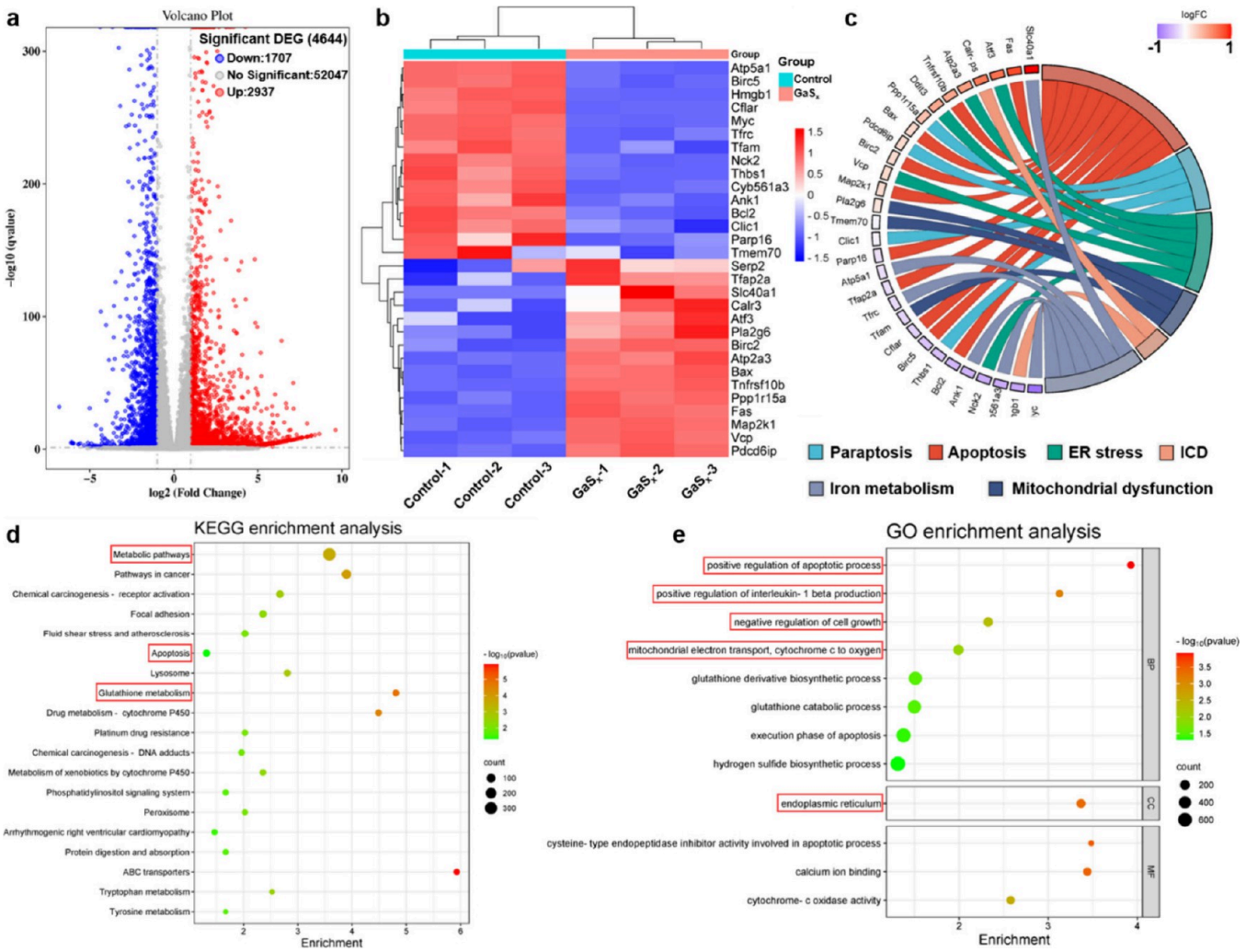

Figure 5. Gene expression correlation and differential gene expression analysis of CT26 cells before and after GaS_x treatment. (a) Volcano plots of differentially expressed genes before and after GaS_x treatment (Red dots: up-regulated genes, blue dots: down-regulated genes, and gray dots: nondifferentially expressed genes). (b) Clustering heatmap of the 15 up-regulated and 15 down-regulated differential genes (Red color: high expression of the gene; blue color: low expression of the gene). (c) Enrichment of GO terms in the chordal graph. (d) KEGG pathway enrichment analysis of 15 up-regulated and 15 down-regulated differential genes. (e) Bioprocess GO enrichment analysis of 15 up-regulated and 15 down-regulated differential genes.

penetration and activation of immune cells. As an essential component of the immune system, dendritic cells (DCs) mature upon stimulation by DAMPs signals, followed by antigen capture and presentation. The stimulation of DCs maturation by the supernatant of CT26 cells was next examined after GaS_x incubation. It was found that the proportion of matured DCs increased in a concentration-dependent manner after incubation with the supernatant of CT26 cells treated with GaS_x, indicating the effectiveness of GaS_x in activating the immune response (Figure 4j and 4k). The above results confirmed that GaS_x induced the paraptosis−apoptosis hybrid pathway by disrupting iron metabolism. While previous research has highlighted the link between iron metabolism and apoptosis, the connection between iron metabolism and paraptosis has largely been overlooked. GaS_x-induced paraptosis holds distinct advantages over classical apoptosis, such as circumventing apoptotic resistance and stimulating immune responses (Figure 4l). Therefore, GaS_x holds significant promise to synergize with other clinical therapies, such as chemotherapy and immunotherapy.

2.5. Ranscriptome Sequencing of GaS_x Treated CT26 Cells. To further confirm the mechanism of GaS_x on disrupting iron metabolism and killing CT26 cells, transcriptome sequencing was performed on the cells preand post-GaS_x treatment. Compared with the control group, there were 4644 differentially expressed genes in the GaS_x group, containing 1707 down-regulated and 2937 up-regulated genes (Figure 5a). To elucidate the roles of these genes, a subset of 30 genes (with 15 down-regulated and 15 up-regulated genes) was specifically highlighted. A heatmap showed that these 30 target genes were consistently up or down-regulated in all the samples from the GaS_x group compared to those from the control group (Figure 5b). Furthermore, to crystallize the identification of genes governing these described functions, enrichment chord diagrams were rendered for further graphic analysis. The main functions of the target genes in the two differential enrichment analyses mainly focused on ER stress, mitochondrial dysfunction, apoptosis, and paraptosis (Figure 5c). Specifically, the heightened expression of stress-associated ER

https://doi.org/10.1021/acsnano.4c06199
ACS Nano XXXX, XXX, XXX−XXX

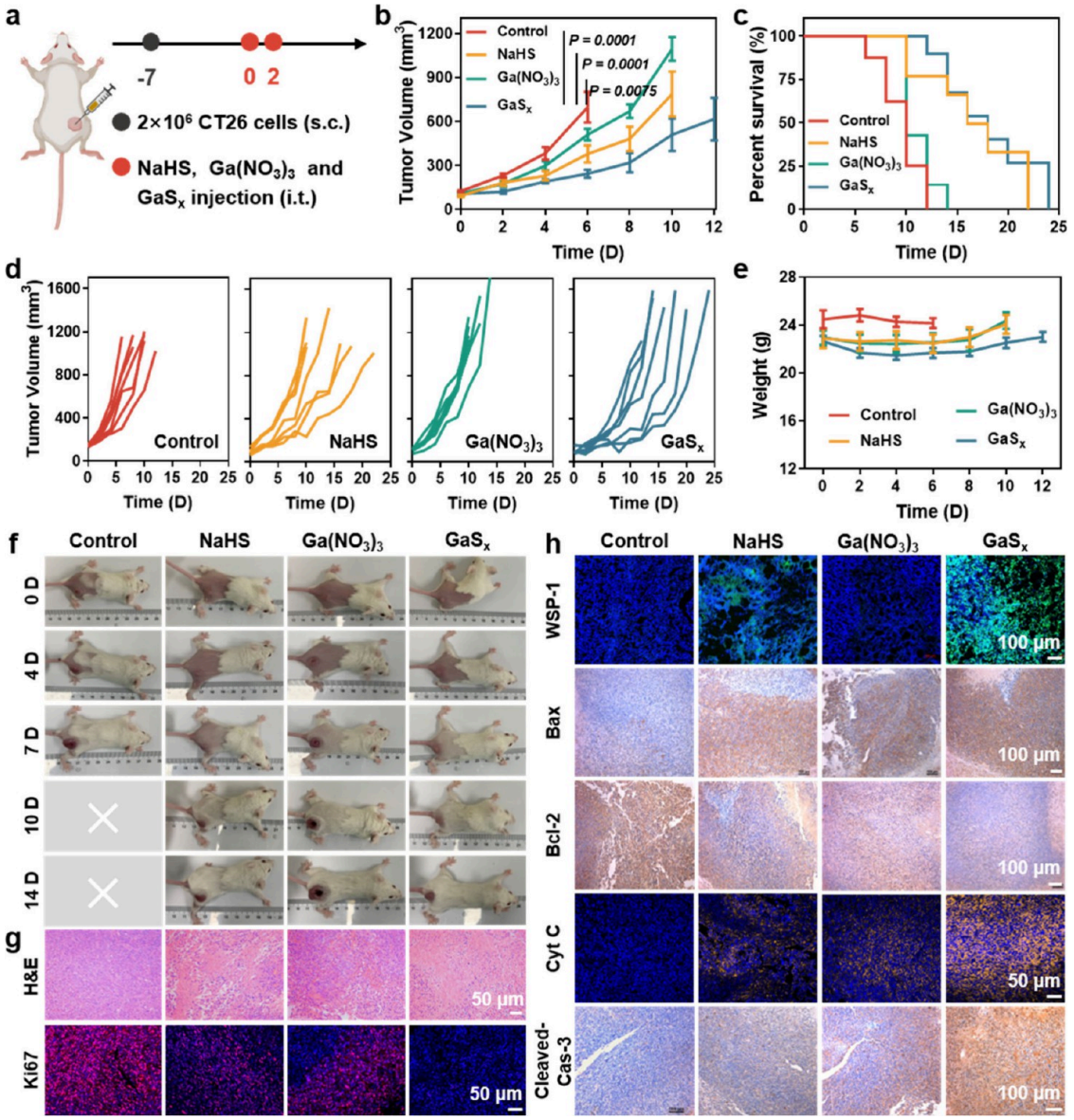

Figure 6. *In vivo* antitumor therapy with GaS_x. (a) Scheme of the NaHS, $Ga(NO_3)_3$, and GaS_x treatments. (b) Tumor volume of the mice in each group in (a) (n = 7). (c) Survival curves of mice after different treatments in (a). (d) Tumor volumes of the mice after different treatments in (a). (e) Body weights of the mice after various treatments in (a). (f) Photographs of tumors in mice after various treatments in (a). (g) H&E images and Ki67 stained tumors after different treatments. (h) Confocal images of WSP-1 probe and Cyt C immunofluorescence stained tumors after different treatments; Immunohistochemical images of Bax, Bcl-2 and cleaved caspase-3 stained tumors after different treatments.

protein family member 2 (Serp2) corroborated the induction of ER stress by GaS_x (Figure 4d). Moreover, the down-regulation of key genes involved in maintaining normal ATP synthase function (Tmem70) and genes encoding key mitochondrial transcription factors (Tfam) also confirmed that GaS_x-caused mitochondrial dysfunction (Figure 4b). The expression of Bax, Fas, and Tnfrsf10b, which were involved in the positive regulation of apoptosis, was up-regulated after GaS_x treatment. Simultaneously, the expression of genes such as Bcl2, Birc5, and Parp1, which were involved in the negative regulation of cell proliferation, was down-regulated. These results demonstrated that GaS_x led to ER stress and mitochondrial dysfunction by disrupting iron metabolism, ultimately inducing both apoptosis and paraptosis. Moreover, the immunogenic cell death (ICD) associated gene, Hmgb1, was down-regulated in the GaS_x group (Figure 5b and 5c), further confirming the effectiveness of GaS_x in releasing DAMPs by inducing paraptosis.

Subsequently, the functions of these 30 target genes were investigated using Gene Ontology (GO) and Kyoto Encyclopedia of Genes and Genomes (KEGG) enrichment analysis. The horizontal axis represents the enrichment factor, hinting that a more considerable factor indicates higher enrichment levels. The bubble size depicted the gene count, while the color gradient of the bubbles corresponded to different adjustment (adjusted P-value) ranges. According to the KEGG enrichment analysis, the target genes were mainly concentrated in metabolic pathways, GSH metabolism, and apoptosis (Figure 5d). The GO analysis revealed a predominant enrichment of target genes in processes such as

https://doi.org/10.1021/acsnano.4c06199
ACS Nano XXXX, XXX, XXX−XXX

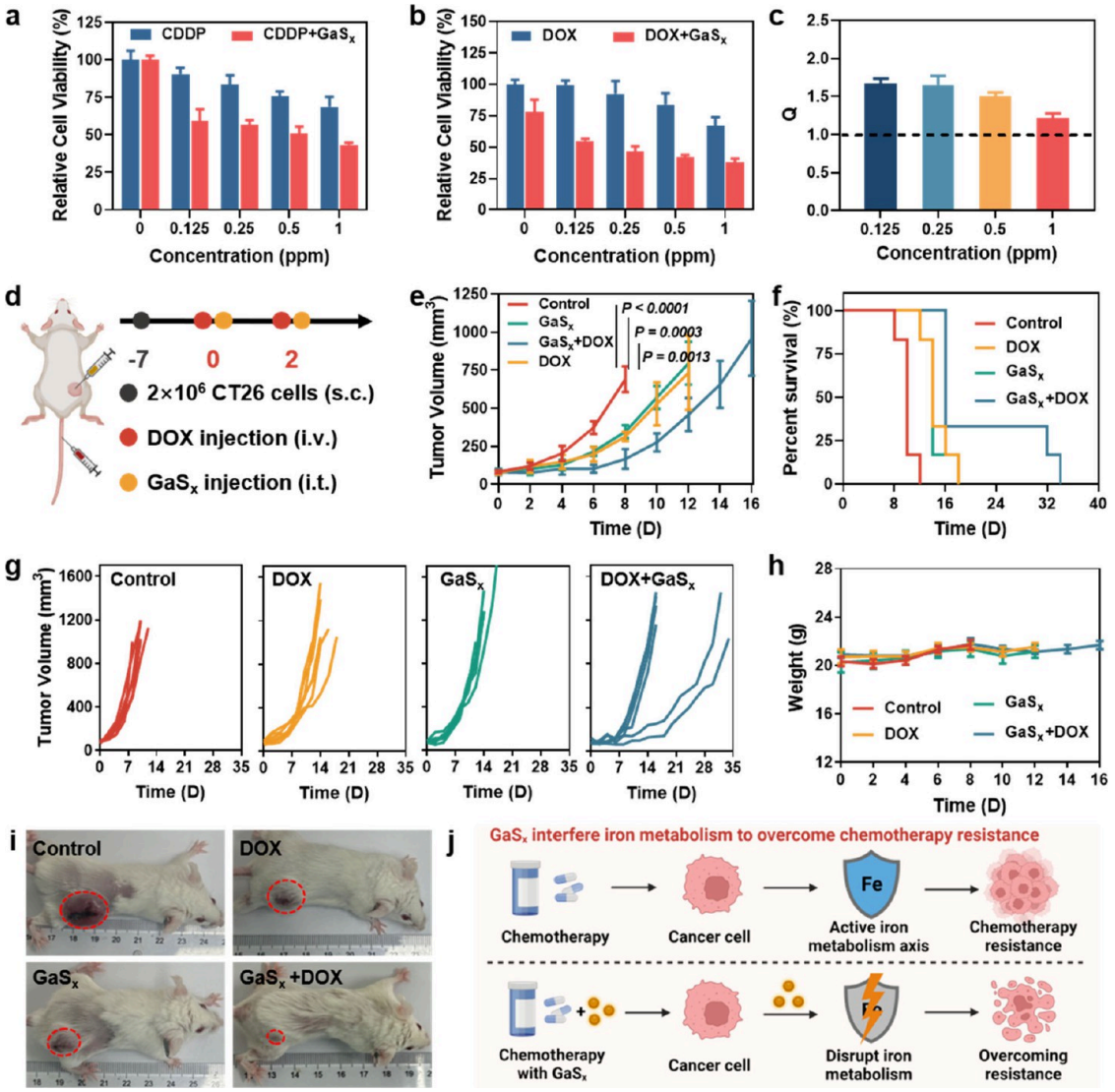

Figure 7. Synergistic effect of GaS_x on chemotherapy. (a) Combined cell killing effect of GaS_x and different concentrations of CDDP. (b) Combined cell killing effect of GaS_x and different concentrations of DOX. (c) Synergistic effects (Q) of the combinations of GaS_x and DOX with different concentrations on cell death in (b). (d) Scheme of combined GaS_x and DOX treatment. (e) Tumor volume of the mice in each group in (d). (f) Survival curves of mice after different treatments in (d). (g) Tumor volume of the mice after different treatments in (d). (h) Body weights of the mice after various treatments in (d). (i) Photographs of tumors in mice after various treatments in (d). (j) Scheme of the mechanism by which GaS_x interferes with iron metabolism to overcome chemotherapy resistance.

cytochrome c release, interleukin-1β release, negative regulation of cell growth, and apoptosis (Figure 5e). Collectively, the above data suggested the profound impact of GaS_x on the regulation of key proteins involved in iron metabolism, ER stress, mitochondrial dysfunction, apoptotic pathways, and the efficacious triggering of pathways that underlie tumor cell eradication and immune activation.

2.6. Antitumor Effects Mediated by GaS_x. Encouraged by the promising ability of GaS_x to disrupt iron metabolism and induce paraptosis and apoptosis *in vitro*, we further validated the *in vivo* antitumor effect of GaS_x. CT26 tumor-bearing mice were randomly assigned into four groups: (1) Control, (2) NaHS, (3) $Ga(NO_3)_3$, and (4) GaS_x. Various formulations were administered by intratumoral (i.t.) injection at a dose equivalent to 5 mg/kg on days 0 and 2 (Figure 6a). It was observed that $Ga(NO_3)_3$ treatment had a limited effect in inhibiting tumor growth (Figure 6b), suggesting that iron interference therapy using $Ga(NO_3)_3$ might not sufficiently inhibit tumor growth, as it failed to overcome the competition posed by the abundant iron present within the tumor. Moreover, moderate tumor growth inhibition was noted with NaHS treatment, which was ascribed to the interplay between H_2S and iron metabolism as well as the repression of mitochondrial function in cancer cells (Figure 6b and 6d). Furthermore, the mice treated with GaS_x showed a substantially slower tumor growth rate than the other groups, pointing to the potent antitumor action of GaS_x. As a result, the median survival time of the mice treated with GaS_x was extended to 16 days, which was significantly greater than that of the control group (8 days) (Figure 6c). These results suggested that GaS_x-mediated iron interference was an effective tumor therapy strategy. Importantly, the body weights of the mice did not obviously decrease in any of the groups, and no obvious damage was observed in the hematoxylin-eosin stained (H&E) sections of the major organs (heart, liver, spleen, lungs and kidneys) of the mice after the various

https://doi.org/10.1021/acsnano.4c06199
ACS Nano XXXX, XXX, XXX−XXX

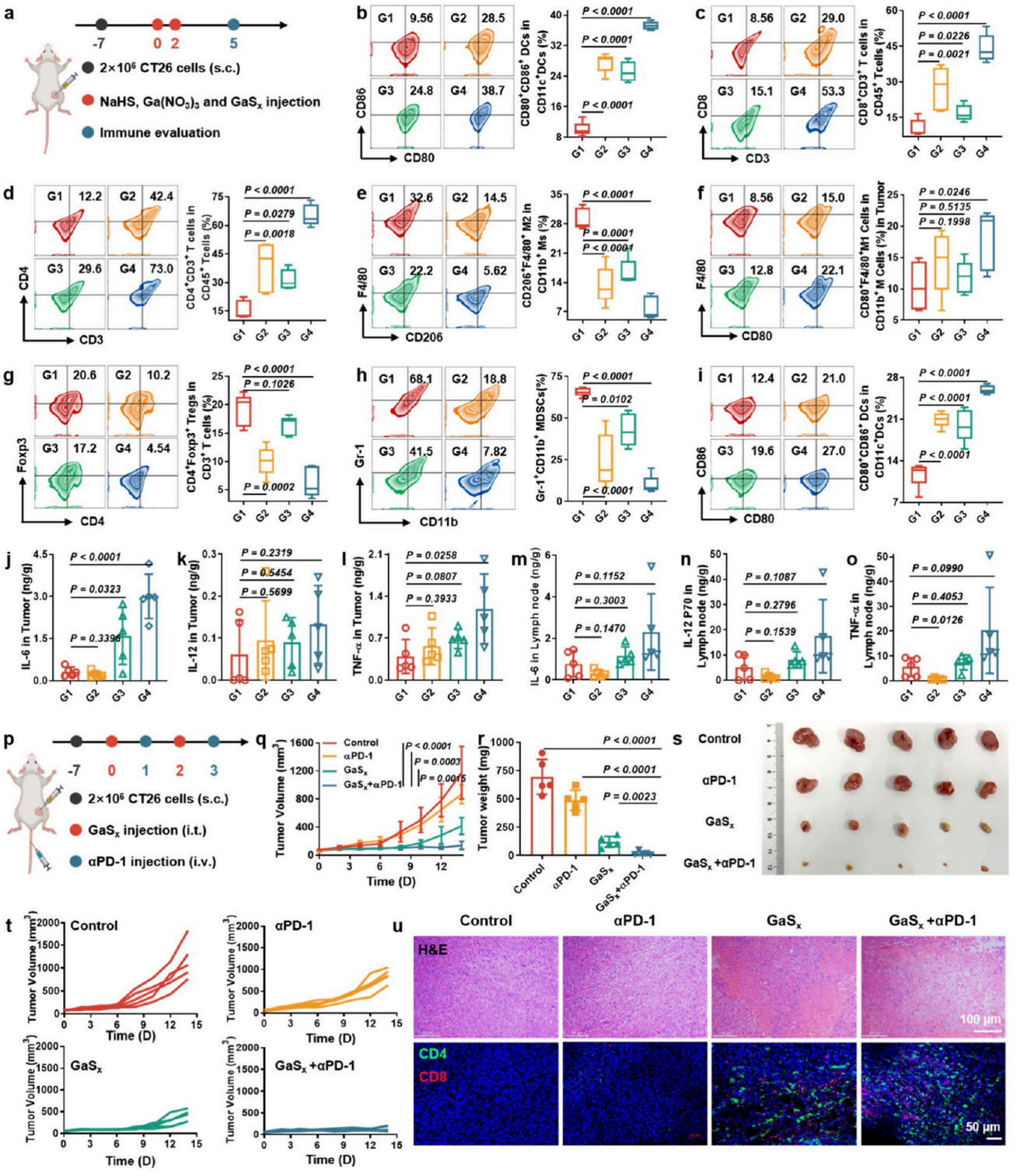

Figure 8. Immunological evaluation of tumors from GaS_x-treated mice and the combination therapy with GaS_x and αPD-1 antibody. (a) Scheme of the immuno-evaluation of tumors and TDLNs after different treatments (G1: Control, G2: NaHS, G3: $Ga(NO_3)_3$, and G4: GaS_x). (b) Mature DCs in tumors after different treatments in (a). (c) $CD8^+$ T cells infiltration in tumors after different treatments in (a). (d) $CD4^+$ T cell infiltration in mouse tumors after various treatments in (a). (e) Proportion of M2 cells in tumors after various treatments in (a). (f) Proportion of M1 cells in mouse tumors after various treatments in (a). (g) Tregs infiltration in mouse tumors after various treatments in (a). (h) Proportion of MDSCs in mouse tumors after various treatments in (a). (i) Mature DCs in TDLNs after different treatments in (d). (j–l) Pro-inflammatory cytokine levels (j) IL-6, (k) IL-12p70, and (l) TNF-α in tumors from the mice after various treatments in (a). (m–o) Pro-inflammatory cytokine levels (m) IL-6, (n) IL-12p70, and (o) TNF-α in the TDLNs of the mice after various treatments are shown in (a). (p) Scheme of GaS_x and αPD-1 combination therapy. (q) Tumor volume of the mice in each group ($n = 5$) in (p). (r) Tumor weights of the mice after 14 days of different treatments in (p). (s) Photographs of tumors after 14 days of different treatments in (p). (t) Tumor volume of mice after different treatments in (p). (u) H&E images and $CD4^+$ $CD8^+$ stained tumors after 14 days of different treatments in (p).

https://doi.org/10.1021/acsnano.4c06199
ACS Nano XXXX, XXX, XXX−XXX

treatments (Figure 6e and Supporting Figure S19), indicating the negligible physiological toxicity of GaS_x. This difference was mainly attributed to the difference in iron metabolism between cancer cells and normal cells, underpinning the selectivity and safety of GaS_x.

To further investigate the mechanism of the anticancer effects of the various treatments, the tumor tissues were collected for immunohistochemical and immunofluorescence staining analysis on day 4 post-treatment. WSP-1 staining of tumor sections showed revealed marked green fluorescence in the GaS_x group, indicating that GaS_x could effectively decompose and continuously release H_2S at tumor sites (Figure 6h). These findings suggested that GaS_x was biologically active *in vivo* and provided conducive conditions for disrupting iron metabolism in tumor cells. H&E staining revealed aberrations in the nuclei of the tumor cells treated with $Ga(NO_3)_3$ and NaHS, as some of the cells appeared rounded and crinkled, indicating that both Ga^{3+} and H_2S only moderately damaged the tumor cells. Notably, almost all the tumor cells were wrinkled or even absent in the GaS_x group, indicating the excellent tumor damage effect of GaS_x (Figure 6g). Ki67 fluorescence staining demonstrated a minimal amount of red fluorescence signal in the GaS_x group, illuminating a striking contrast to the other groups. This observation intimates that GaS_x exerts the most potent inhibitory effect on tumor cell proliferation (Figure 6g).

Additionally, in comparison to the other groups, treatment with GaS_x significantly upregulated the expression of the Bax protein on the mitochondrial outer membrane while concurrently downregulaing the expression of the Bcl-2 protein (Figure 6h). These alterations implied that GaS_x invoked mitochondrial distress by interfering with iron homeostasis within tumor cells. As a result, GaS_x treatment facilitated the substantial release of Cyt C into the cytoplasm and initiated the activation of caspase-3, as evidenced by the elevated levels of Cyt C and the increased presence of cleaved caspase-3 in the GaS_x group (Figure 6h). These observations provided strong evidence that GaS_x was capable of inducing mitochondrial impairment and triggering tumor cell death through the disruption of iron metabolism.

2.7. Synergistic Effect of GaS_x on Chemotherapy. GaS_x has demonstrated a good capacity to directly destroy tumors by disrupting iron metabolism. Notably, the aberrant iron metabolic pathways in tumors presents a formidable challenge to numerous clinical therapies.[43] Consequently, GaS_x holds considerable promise for enhancing the efficacy of anticancer treatments, especially those aimed at overcoming resistance associated with iron metabolism. Chemotherapy remains one of the most prevalent treatments for cancer in clinical settings. However, cancer cells may exploit iron as a defensive mechanism against the cytotoxic effects of treatment during chemotherapy. Iron's role in gene regulation and in shaping the tumor microenvironment can significantly influence the outcome of cells subjected to chemotherapeutic drugs.[44,45] Due to the powerful disruption of iron metabolism by GaS_x and its ability to induce paraptosis, it is expected to dramatically improve the effectiveness of chemotherapy. In light of these findings, we delved further into the potential synergistic benefits of combining GaS_x with standard chemotherapy drugs such as doxorubicin (DOX) and CDDP. GaS_x demonstrated enhanced synergistic effects on both CDDP and DOX, particularly with DOX (Figure 7a and 7b, Supporting Figure S20). At concentrations of DOX at 0.125, 0.25, 0.5, and 1 ppm, the cell killing rates were 0.6%, 7.8%, 16.3%, and 32.9%, respectively. However, when GaS_x was used at a low concentration, there was a sharp increase in cell mortality to 49.5%, 58.0%, 58.3% and 69.3%, with the synergy coefficients (Q) of 1.67 ± 0.07, 1.65 ± 0.12, 1.51 ± 0.05, and 1.22 ± 0.05, respectively (Figure 7b and 7c). These findings compellingly supported the profound cooperative interaction between GaS_x and DOX. Encouraged by the *in vitro* good tumor cell killing effect of GaS_x combined with DOX, we further explored the combined antitumor effect of these agents *in vivo*. Compared with single GaS_x or DOX treatment, the combination of GaS_x and DOX had excellent antitumor effects without noticeable toxic side effects. Taken together, these results indicated that the disruption of iron metabolism by GaS_x significantly bolstered the therapeutic potency of DOX, thereby extending the lifespan of mice bearing tumors (Figure 7d−7i). Therefore, GaS_x not only eliminated tumor cells through the disruption of iron metabolism, but also assisted chemotherapy in overcoming the obstacles posed by iron-related chemotherapy resistance, efficaciously magnifying the therapeutic impact and providing more effective avenues for shaping future clinical chemotherapy protocol designs (Figure 7j).

2.8. Synergistic Effect of GaS_x on Immunotherapy. Inadequate immune cell infiltration and an activated immunosuppressive microenvironment are important causes of clinical immunotherapy failure. Enhancing the immunogenicity of tumors and reversing the immunosuppressive microenvironment are the keys to improving the efficacy of immunotherapy. The mode of cancer cell death induced by GaS_x is intricately linked to the dual processes of apoptosis and paraptosis, with the latter being particularly effective at stimulating the immune system through the release of DAMPs. Moreover, iron plays a vital role in the function of the immune system, and disrupting iron metabolism within tumors could reshape the properties and capabilities of tumor-infiltrating immune cells.[43] Therefore, GaS_x has the potential to act as a powerful immunomodulator, markedly influencing the immune milieu within tumors by modulating tumor iron metabolism and inducing paraptosis, which could prime the tumor for heightened sensitivity to immunotherapy.

To investigate the immunological consequences of GaS_x treatment, the composition and infiltration ratio of immune cells in tumors and tumor-draining lymph nodes (TDLNs) were analyzed 72 h after GaS_x administration (Figure 8a). The proportions of mature DCs in tumors after NaHS and $Ga(NO_3)_3$ treatments increased from ∼9.56% to ∼28.5% and ∼24.8%, respectively. Moreover, following GaS_x treatment, the proportion of mature DCs increased even further to 38.7%, which was 3.9 times greater than that in the control group (Figure 8b). These findings suggested that GaS_x induced tumor cells to release DAMPs, thereby stimulating DCs maturation, which was a foundational step for initiating an immune response. Moreover, GaS_x demonstrated the strongest effect on enhancing the infiltration of both $CD4^+$ and $CD8^+$ T cells. The proportions of $CD4^+$ and $CD8^+$ T cells in the GaS_x group increased to ∼73.0% and ∼53.3%, respectively, far surpassing the levels in the control, NaHS, and $Ga(NO_3)_3$ groups (Figure 8c and 8d). These results robustly endorse the capacity of GaS_x to activate the T cell-mediated immune response through the induction of paraptosis.

Interestingly, GaS_x therapy profoundly affected tumor-associated macrophage phenotypes. Specifically, within the immunologically suppressive microenvironment of the tumor,

https://doi.org/10.1021/acsnano.4c06199
ACS Nano XXXX, XXX, XXX−XXX

the control group displayed a substantial prevalence of M2 macrophages, with the proportions as high as ~32.6% (Figure 8e). In stark contrast, GaS_x treatment strongly reduced the proportion of M2 macrophages within the tumor, plummeting to a mere ~5.62%. Correspondingly, compared with those in the control group, the percentage of pro-inflammatory M1 macrophages in the GaS_x-treated group increased 2.6-fold, reaching ~22.1% (Figure 8f). These results strongly confirmed the potent capability of GaS_x to induce a paradigm shift in TAM phenotypes from the suppressive M2 phenotype to the inflammatory M1 phenotype. This interesting shift in macrophage phenotype was intricately associated with iron availability.[46,47] A deficit of iron steers macrophages toward the M2 type, while an adequate iron supply favors M1 polarization.[48] GaS_x adeptly impeded the uptake of iron by tumor cells, thereby ensuring a surplus of iron that favors M1 macrophage polarization. Furthermore, other single-agent therapies, including NaHS and $Ga(NO_3)_3$, also supported TAM M1 polarization to a degree, reinforcing the concept that disrupting iron metabolism within tumors is conducive to M1 macrophage polarization.

Moreover, GaS_x therapy significantly diminished the presence of regulatory T cells (Tregs) and myeloid-derived suppressor cells (MDSCs) in tumor, which are infamous for establishing the immunosuppressive microenvironment of solid tumors and contribute to the frequent failure of immunotherapies. After GaS_x administration, the infiltration percentages of Tregs and MDSCs decreased to ~4.54% and ~7.82%, respectively, significantly undercutting those observed in the control group (Figure 8g and 8h). Since NaHS treatment similarly resulted in a noticeable reduction in Tregs and MDSCs, while $Ga(NO_3)_3$ had a minimal impact, the reduction in Tregs and MDSCs effected by GaS_x was likely attributable to the modulatory impact of H_2S gas on the immune microenvironment. GaS_x therapy thus disrupted the immune balance within tumors by boosting pro-immune cell infiltration and reducing suppressive cell presence, provoking a strong immune reaction. After GaS_x treatment, significant increases in pro-inflammatory cytokines, such as interleukin-6 (IL-6), interleukin-12p70 (IL-12p70), and tumor necrosis factor-alpha (TNF-α), were observed in the tumors and the TDLNs (Figure 8j–8o). Additionally, there was a marked increase in the proportion of mature DCs in the TDLNs after GaS_x therapy, indicating enhanced lymphocyte homing, a critical process for augmenting systemic antitumor immune responses (Figure 8i). Consequently, by disrupting tumor iron metabolism, GaS_x not only triggered paraptosis to promote the release of DAMPs and activate the immune response, but also altered iron distribution within the tumor microenvironment, driving M1 macrophage polarization. This approach is anticipated to significantly enhance the efficacy of immunotherapeutic approaches.

To further explore the potentiating effect of GaS_x on immunotherapy, we combined GaS_x with αPD-1, a prevalent immune checkpoint inhibitor in clinical use. CT26 tumor-bearing mice were administered i.t. injections of GaS_x on days 0 and 2, and i.v. injections of αPD-1 on days 1 and 3 (Figure 8p). The efficacy of αPD-1 in inhibiting tumor growth was greatly restricted due to minimal T cell infiltration within solid tumors (Figure 8q–8t, Supporting Figure S21). However, GaS_x not only directly damaged tumors by disrupting iron metabolism, but also elevated T cells infiltration by activating the antitumor immune response. Consequently, GaS_x compensated for the deficiency of αPD-1 and synergized to significantly impede tumor progression when used in combination with αPD-1. Due to the specific destruction of iron metabolism by GaS_x on tumors, combination therapy with αPD-1 and GaS_x showed good biosafety, as evidenced by the stable body weight of the treated mice (Supporting Figure S22). Moreover, H&E-stained tumor sections from the different groups were analyzed to verify the extent of tumor cell damage. The number, size and morphology of the nuclei in the αPD-1 group were similar to those in the control group. However, the dual treatment of GaS_x combined with αPD-1 induced more pronounced tissue destruction, noticeable by a substantial reduction in nuclear count and nucleus condensation (Figure 8u). Moreover, the proliferation of tumor cells was significantly more inhibited in the GaS_x + αPD-1 group than treatment with GaS_x or αPD-1 alone (Supporting Figure S23). Furthermore, $CD4^+$ and $CD8^+$ T cell infiltration levels were also examined after the different treatments. The tumor sections revealed an appreciable increase in red and green fluorescent signals indicative of $CD4^+$ and $CD8^+$ T cell infiltrations after GaS_x treatment, and this infiltration was further amplified when GaS_x was used in combination with αPD-1 (Figure 8u). These results strongly supported the effectiveness of combining GaS_x with immunotherapy. The above results confirmed the potential of GaS_x in enhancing clinical immune therapy efficacy. On one hand, GaS_x disrupted iron metabolism, triggering paraptosis and DAMPs release. On the other hand, it induced M1 polarization of macrophages by altering the intratumoral iron distribution and suppressed the infiltration of MDSCs and Tregs through H_2S-mediated signaling regulation. This synergistic approach significantly bolstered tumor immunogenicity and reversed the immunosuppressive tumor microenvironment, effectively overcoming the obstacles of immune therapy.

3. CONCLUSIONS

Bioactive GaS_x with dual functions of "reprogramming" and "interfering" iron metabolic pathways, was developed for tumor iron metabolism therapy. These nanodots utilize H_2S, which was released within the tumor microenvironment, to reprogram the iron metabolism axis in cancer cells. By down-regulating TfR1 and up-regulating FPN1 expression, the intracellular Fe concentration was reduced. Moreover, Ga^{3+} released from GaS_x acted as a biochemical "Trojan horse" that substituted for Fe stations and displaced Fe from important biomolecule-binding sites. GaS_x exploited a dual mechanism of Ga^{3+}-mediated iron destruction and H_2S-promoted reprogramming of iron metabolic pathways to induce mitochondrial dysfunction and ER stress, leading to paraptosis in tumor cells. GaS_x inhibited the repair and proliferation of tumor cells by ectopic induction of Endo G and PARP1. It also upregulated the apoptosis-inducing factors AIF, Bax, and cleaved caspase-3, activating both caspase-3-dependent and caspase-3-independent apoptotic pathways. GaS_x induced the initiation of a mixed apoptotic-paraptotic pathway in cancer cells, which resulted in a significant inhibition of tumor proliferation. Importantly, GaS_x-induced dysregulation of iron metabolism significantly increased the sensitivity of tumor cells to chemotherapy and immune checkpoint blockade therapy. This research convincingly confirms the potential interplay among iron metabolism, paraptosis, and the immune response, offering insights for advancing clinical therapies and crucial insight for developing more productive cancer treatment modalities.

https://doi.org/10.1021/acsnano.4c06199
ACS Nano XXXX, XXX, XXX−XXX

4. EXPERIMENTAL SECTION

4.1. Synthesis and Characterization. *4.1.1. Materials.* 1-dodecanethiol was purchased from Aladdin, 1-octadecene (ODE) was purchased from Aladdin, and oleylamine (OM) was purchased from Sigma. Paraptosis inhibitor (cycloheximide, CHX) purchased from MedChemExpress (Monmouth Junction, NJ, USA). SDS-polyacrylamide gel electrophoresis (SDS-PEG) gels were purchased GenScript. RPMI 1640 medium was purchased from Vivacell Shanghai, China. Fetal Bovine Serum was purchased from Inner Mongolia Opcel Biotechnology Co.,Ltd.

4.1.2. Synthesis of GaS_x. Briefly, 0.75 mmol of gallium acetylacetonate (278 mg) and 150 mg of sublimed sulfur were placed in a three-necked flask, and 9 mL of ODE, 3 mL of OM, 3 mL of OA, and 3 mL of 1-dodecanethiol were added and mixed while stirring at room temperature. Next, the above system was slowly heated up to 130 °C under N_2 protection and kept for 20 min to remove air and H_2O. Next, the mixture was further heated up to 270 °C and the reaction was carried out for 15 min, and the mixture was subsequently cooled to room temperature to obtain GaS_x.

200 μL of GaS_x was added to a 2 mL EP tube (PROMETHE Biotechnology), 2 mL of anhydrous ethanol was added, the mixture was centrifuged at 14800 rpm for 5 min, and the supernatant was discarded to obtain the GaS_x precipitate. Next, the obtained GaS_x was washed with an ethanol: cyclohexane = 10:1 (V:V) wash solution under US conditions and centrifuged at 14800 rpm for 5 min, after which the supernatant was discarded. GaS_x was cleaned five times as described above to remove OED, OM, OA and 1-dodecanethiol from the surface to obtain the cleaned GaS_x.

4.1.3. Detection of H_2S Release from GaS_x. 4.1.3.1. Lead Acetate Test Paper Detection. Different concentrations of GaS_x were placed in 13 mm cell culture dishes, lead acetate detection test paper wetted with H_2O was placed on the lids of the cell culture dishes, and a sealing film was used to create an airtight environment. The above cell culture dishes were placed in a 37 °C oven, and the change in color of the lead acetate test paper in each group was observed 2 h later.

4.1.3.2. WSP-1 Probe Detection. GaS_x was dispersed in different pH buffers and incubated with the wsp-1 probe for 30 min. Next, the fluorescence signals of each group were detected with a microplate reader; GaS_x was incubated with different concentrations of GSH and with the wsp-1 probe for 30 min. Next, the fluorescence signals of each group were detected with a microplate reader.

4.1.4. Ion Release Detection of GaS_x. GaS_x was dispersed in different pH buffers and placed in a dialysis bag. The liquid in the external environment was removed at different time, and the concentration of Ga^{3+} was measured by ICP-MS.

GaS_x was coincubated with GSH and placed in a dialysis bag. The liquid in the external environment was removed at different time, and the concentration of Ga^{3+} was measured by ICP-MS.

4.2. In Vitro Experiments. *4.2.1. Effect of GaS_x on Iron Metabolism.* 3×10^6 HeLa cells were inoculated in 10 mm cell culture dishes and incubated for 24 h to ensure the cells were adherent. NaHS (0.636 mM), $Ga(NO_3)_3$ (0.424 mM) and GaS_x (50 ppm) were added respectively and incubated for 24 h. The supernatant was discarded, and 1 mL of western and IP cell lysates was added. The mixture was subsequently lysed for 30 min. Next, the protein concentration was determined by centrifugation at 12000 rpm for 15 min using a BCA kit. Changes in the expression of TfR1 and FPN1, key proteins involved in the Fe transport process, were detected in each group of proteins via WB.

4.2.2. GaS_x Induced Paraptosis in Tumor Cells. CT26 and HeLa cells were inoculated in 24-well plates at a density of 2×10^5 cells/well and incubated for 12 h to ensure that the cells were adherent to the wall. The cells were incubated with 25, 50, and 100 ppm GaS_x for 24 h. The morphology of CT26 and HeLa cells in each group was observed by an inverted fluorescence microscope.

4.2.3. Detection of GaS_x-Induced Paraptosis-Related Proteins. 3×10^6 CT26 cells were inoculated in a 10 mm cell culture dish and incubated for 24 h to ensure that the cells adhered to the wall. The cells were incubated with 25, 25, and 100 ppm GaS_x for 24 h. Next, the supernatant was discarded, and 1 mL of western and IP cell lysate was added and lysed for 30 min. Next, the protein concentration was determined by centrifugation at 12000 rpm for 15 min using a BCA kit. Changes in the expression of the paraptosis-related proteins eif2α/p-eif2α and CHOP in each group of proteins were detected via WB analysis.

4.2.4. Endoplasmic Reticulum Stress Induced by GaS_x. CT26 cells were inoculated in 15 mm glass bottom cell culture dish (NEST Biotechnology) at a density of 2×10^5 cells/well and incubated for 12 h to ensure cell adhesion. Then 25 ppm of GaS_x was added, and the mixture was incubated for 12 h and then washed with precooled HBSS. After that, 1:2000 diluted ER-Tracker Geen was added and incubated for 1 h. Next, the cells were washed with 1640 medium and incubated for 10 min with Hoechst 33342 live cell staining solution. Endoplasmic reticulum stress in the cells was observed with a Zeiss confocal microscope.

4.2.5. Assay of Mitochondrial Swelling Induced by GaS_x. CT26 cells were inoculated in 15 mm glass bottom cell culture dish (NEST Biotechnology) at a density of 2×10^5 cells/well and incubated for 12 h to ensure cell adhesion. Then, 25 ppm of GaS_x was added, and the mixture was incubated for 12 h and then washed with precooled HBSS. After that, 1:2000 diluted Mito-Tracker Deep Red was added and incubated for 1 h. Next, the cells were washed with 1640 medium and incubated for 10 min with Hoechst 33342 live cell staining solution. Mitochondrial swelling in the cells was observed with a Zeiss confocal microscope.

4.2.6. GaS_x Induced Apoptosis. CT26 cells were inoculated in 24-well plates at a density of 2×10^5 cells per well and incubated for 12 h to ensure that the cells were adherent. NaHS (0.636 mM), $Ga(NO_3)_3$ (0.424 mM) and GaS_x (50 ppm) were added, and the mixture was incubated for 24 h. The supernatant was discarded, and the cells were washed with PBS. Next, the cells were stained with an Annexin V FITC/PI Apoptosis Detection Kit (BeiJing Solarbio Science & Technology Co., Ltd.), and the fluorescence signals of each group were detected by flow cytometry (FongCyte, Challenbio).

4.3. In Vivo Experiments. *4.3.1. GaS_x Treatment of CT26 Tumors.* 6−8-week female Balb/c mice were injected subcutaneously (s.c.) with 2×10^6 CT26 cells, and when the average tumor volume reached 100 mm^3 the mice were randomly divided into the following four groups: 1) control, 2) NaHS (6.02 mg/kg), 3) Ga^{3+} (5 mg/kg), and 4) GaS_x (5 mg/kg), with seven mice in each group. The mice were treated on days 0 and 2, after which the tumor volume and mouse body weight were recorded every 2 days.

4.3.2. Tumor Immune Evaluation after Intratumoral Injection of GaS_x. 6−8-week female balb/c mice were injected (s.c.) with 2×10^6 CT26 cells, and subsequent experiments were performed when the tumor volume reached approximately 100 mm^3. The mice were randomly divided into four groups of 5 mice each, 1) control, 2) NaHS (i.t., 6.02 mg/kg), 3) Ga^{3+} (i.t., 5 mg/kg), and 4) GaS_x (i.t., 5 mg/kg), and were injected on days 0 and day 2, respectively. The mice were sacrificed on day 4, and the tumors and lymph nodes were collected, and the cells were harvested after digestion with digestive enzymes. The DCs maturation, T cell infiltration level, tumor-associated macrophage level, Tregs cell level, and infiltration of MDSCs into the tumor site were determined, as well as the level of DCs maturation at the lymph node.

ASSOCIATED CONTENT

Supporting Information

The Supporting Information is available free of charge at https://pubs.acs.org/doi/10.1021/acsnano.4c06199.

Additional experimental steps including GaS_x modification, degradation detection of GaS_x, verification of iron importance, endocytosis, detection of intracellular H_2S release and Ga/Fe content, detection of GaS_x-induced apoptosis-related proteins, GaS_x-enhanced DOX treatment of CT26 tumors, GaS_x potentiated the α-PD-1 treatment of CT26 tumors and Supporting Figures S1−S23 (PDF)

https://doi.org/10.1021/acsnano.4c06199
ACS Nano XXXX, XXX, XXX−XXX

AUTHOR INFORMATION

Corresponding Authors

Guanghui Hou − *Institute of Functional Nano & Soft Materials (FUNSOM), Jiangsu Key Laboratory for Carbon-Based Functional Materials & Devices, Soochow University, Suzhou 215123, China*; Email: ghhou@suda.edu.cn

Liang Cheng − *Institute of Functional Nano & Soft Materials (FUNSOM), Jiangsu Key Laboratory for Carbon-Based Functional Materials & Devices, Soochow University, Suzhou 215123, China*; orcid.org/0000-0001-5324-9094; Email: lcheng2@suda.edu.cn

Authors

Huali Lei − *Institute of Functional Nano & Soft Materials (FUNSOM), Jiangsu Key Laboratory for Carbon-Based Functional Materials & Devices, Soochow University, Suzhou 215123, China*

Lin Liu − *Department of Obstetrics and Gynecology, The First Affiliated Hospital of Soochow University, Suzhou, Jiangsu 215006, China*

Zifan Pei − *Institute of Functional Nano & Soft Materials (FUNSOM), Jiangsu Key Laboratory for Carbon-Based Functional Materials & Devices, Soochow University, Suzhou 215123, China*; orcid.org/0009-0001-6166-9678

Youdong Chen − *Institute of Functional Nano & Soft Materials (FUNSOM), Jiangsu Key Laboratory for Carbon-Based Functional Materials & Devices, Soochow University, Suzhou 215123, China*

Yujie Lu − *Institute of Functional Nano & Soft Materials (FUNSOM), Jiangsu Key Laboratory for Carbon-Based Functional Materials & Devices, Soochow University, Suzhou 215123, China*

Nalin Yang − *Institute of Functional Nano & Soft Materials (FUNSOM), Jiangsu Key Laboratory for Carbon-Based Functional Materials & Devices, Soochow University, Suzhou 215123, China*

Shumin Sun − *Institute of Functional Nano & Soft Materials (FUNSOM), Jiangsu Key Laboratory for Carbon-Based Functional Materials & Devices, Soochow University, Suzhou 215123, China*

Complete contact information is available at: https://pubs.acs.org/10.1021/acsnano.4c06199

Notes

The authors declare no competing financial interest.

ACKNOWLEDGMENTS

This article was partially supported by the National Research Programs of China (2022YFB3804600, 2021YFF0701800), National Natural Science Foundation of China (U20A20254, 52072253, 52302352), Collaborative Innovation Center of Suzhou Nano Science and Technology, Suzhou Key Laboratory of Nanotechnology and Biomedicine, a Jiangsu Natural Science Fund for Distinguished Young Scholars (BK20211544), the 111 Project, Jiangsu Excellent Postdoctoral Project, the China Postdoctoral Science Foundation (2022M722323), and Joint International Research Laboratory of Carbon-Based Functional Materials and Devices, Suzhou Key Laboratory of Nanotechnology and Biomedicine, and Key Laboratory of Structural Deformities in Children of Suzhou (SZS2022018). The authors also thank the website app.Biorender.com for the assistance in creating the illustration.

REFERENCES

(1) Hu, X. M.; Guo, F. F. Amino Acid Sensing in Metabolic Homeostasis and Health. *Endocr. Rev.* **2021**, *42* (1), 56−76.

(2) O'Neill, L. A. J.; Kishton, R. J.; Rathmell, J. A Guide to Immunometabolism for Immunologists. *Nat. Rev. Immunol.* **2016**, *16* (9), 553−565.

(3) Pei, Z. F.; Lei, H. L.; Wu, J.; Tang, W.; Wei, K. L.; Wang, L.; Gong, F.; Yang, N. L.; Liu, L.; Yang, Y. Q.; Cheng, L. Bioactive Vanadium Disulfide Nanostructure with "Dual" Antitumor Effects of Vanadate and Gas for Immune-Checkpoint Blockade-Enhanced Cancer Immunotherapy. *ACS Nano* **2023**, *17* (17), 17105−17121.

(4) Mossmann, D.; Müller, C.; Park, S.; Ryback, B.; Colombi, M.; Ritter, N.; Weissenberger, D.; Dazert, E.; Coto-Llerena, M.; Nuciforo, S.; Blukacz, L.; Ercan, C.; Jimenez, V.; Piscuoglio, S.; Bosch, F.; Terracciano, L. M.; Sauer, U.; Heim, M. H.; Hall, M. N. Arginine Reprograms Metabolism in Liver Cancer via RBM39. *Cell* **2023**, *186* (23), 5068−5083.

(5) Wang, Y.; Gong, F.; Han, Z.; Lei, H.; Zhou, Y.; Cheng, S.; Yang, X.; Wang, T.; Wang, L.; Yang, N.; Liu, Z.; Cheng, L. Oxygen-Deficient Molybdenum Oxide Nanosensitizers for Ultrasound-Enhanced Cancer Metalloimmunotherapy. *Angew. Chem., Int. Ed.* **2023**, *62* (9), No. e202215467.

(6) Palmer, A. E.; Franz, K. J. Introduction to "Cellular Metal Homeostasis and Trafficking. *Chem. Rev.* **2009**, *109* (10), 4533−4535.

(7) Li, C.; Tan, X. L.; Brockman, Q.; Jethava, Y.; Chesi, M.; Bergsagel, P. L.; Chen, F. P.; Frech, I.; Zhan, F. H. Altered Iron Metabolism Is a New Targetable Hallmark for Multiple Myeloma. *Blood* **2019**, *134* (1), 3059.

(8) Sheftel, A. D.; Zhang, A. S.; Brown, C.; Shirihai, O. S.; Ponka, P. Direct Interorganellar Transfer of Iron from Endosome to Mitochondrion. *Blood* **2007**, *110* (1), 125−132.

(9) Kang, N.; Son, S.; Min, S. H.; Hong, H.; Kim, C.; An, J.; Kim, J.; Kang, H. Stimuli-Responsive Ferroptosis for Cancer Therapy. *Chem. Soc. Rev.* **2023**, *52* (12), 3955−3972.

(10) Lang, J. Y.; Zhao, X.; Wang, X. C.; Zhao, Y.; Li, Y. Y.; Zhao, R. F.; Cheng, K. M.; Li, Y.; Han, X. X.; Zheng, X. W.; Qin, H.; Geranpayehvaghei, M.; Shi, J.; Anderson, G. J.; Hao, J. H.; Ren, H.; Nie, G. J. Targeted Co-delivery of the Iron Chelator Deferoxamine and a HIF1α Inhibitor Impairs Pancreatic Tumor Growth. *ACS Nano* **2019**, *13* (2), 2176−2189.

(11) Liu, M.; Liu, B.; Liu, Q. Q.; Du, K. K.; Wang, Z. F.; He, N. Y. Nanomaterial-Induced Ferroptosis for Cancer Specific Therapy. *Coordin. Chem. Rev.* **2019**, *382*, 160−180.

(12) Zhang, C.; Liu, X. Y.; Jin, S. D.; Chen, Y.; Guo, R. H. Ferroptosis in Cancer Therapy: A Novel Approach to Reversing Drug Resistance. *Mol. Cancer* **2022**, *21*, 47.

(13) Knutson, M. D.; Vafa, M. R.; Haile, D. J.; Wessling-Resnick, M. Iron Loading and Erythrophagocytosis Increase Ferroportin 1 (FPN1) Expression in J774 Macrophages. *Blood* **2003**, *102* (12), 4191−4197.

(14) Shi, J. M.; Kong, Y. Y.; Hu, L. N.; Chen, G.; Yu, D. D.; Xie, Y. S.; Wang, Y. C.; Wu, X. S. Ferroportin Downregulation Promotes Cell Proliferation By Modulating the Nrf2-Mir 17−5p Axis in Multiple Myeloma. *Blood* **2019**, *134* (1), 5596.

(15) Zhou, Z.; Gong, F.; Zhang, P.; Wang, X.; Zhang, R.; Xia, W.; Gao, X.; Zhou, X.; Cheng, L. Natural Product Curcumin-based Coordination Nanoparticles for Treating Osteoarthritis via Targeting Nrf2 and Blocking NLRP3 Inflammasome. *Nano Res.* **2022**, *15* (4), 3338−3345.

(16) Moy, B.; Wolff, A. C.; Rumble, R. B.; Allison, K. H.; Carey, L. A. Chemotherapy and Targeted Therapy for Endocrine-Pretreated or Hormone Receptor-Negative Metastatic Breast Cancer and Human Epidermal Growth Factor Receptor 2 Testing in Breast Cancer: ASCO Guideline Rapid Recommendation Update Q and A. *Jco. Oncol. Pract.* **2023**, *19* (8), 547−550.

(17) Faulk, W. P.; Hsi, B. L.; Stevens, P. J. Transferrin and Transferrin Receptors in Carcinoma of the Breast. *Lancet* **1980**, *316* (8191), 390−392.

(18) Liu, D. D.; Dai, X. L.; Zhang, W.; Zhu, X. Y.; Zha, Z. B.; Qian, H. S.; Cheng, L.; Wang, X. W. Liquid Exfoliation of Ultrasmall Zirconium Carbide Nanodots as A Noninflammatory Photothermal Agent in the Treatment of Glioma. *Biomaterials* **2023**, *292*, No. 121917.
(19) Truong, V. K.; Hayles, A.; Bright, R.; Luu, T. Q.; Dickey, M. D.; Kalantar-Zadeh, K.; Vasilev, K. Gallium Liquid Metal: Nanotoolbox for Antimicrobial Applications. *ACS Nano* **2023**, *17* (15), 14406−14423.
(20) Cohen, J.; Denning, D. W.; Evans, E. G. V.; Hay, R. J.; Mackenzie, D. W. R.; Prentice, A. G.; Rogers, T. R. F.; Speller, D. C. E.; Warnock, D. W.; Warren, R. E. Management of Deep Candida Infection in Surgical and Intensive-Care Unit Patients. *Intens. Care. Med.* **1994**, *20* (7), 522−528.
(21) Holbein, B. E.; Ang, M. T. C.; Allan, D. S.; Chen, W. X.; Lehmann, C. Iron-Withdrawing Anti-infectives for New Host-Directed Therapies based on Iron Dependence, the Achilles' Heel of Antibiotic-Resistant Microbes. *Environ. Chem. Lett.* **2021**, *19* (4), 2789−2808.
(22) Pollycove, M.; Maqsood, M. Existence of an Erythropoietic Labile Iron Pool in Animals. *Nature* **1962**, *194* (4824), 152−154.
(23) Fibach, E.; Prus, E. The labile Iron Pool in Normal and Pathological Erythroid Cells Analysis by Flow Cytometry. *Blood* **2005**, *106* (11), 3597.
(24) Zanninelli, G.; Loréal, O.; Brissot, P.; Konijn, A. M.; Slotki, I. N.; Hider, R. C.; Cabantchik, Z. I. The Labile Iron Pool of Hepatocytes in Chronic and Acute Iron Overload and Chelator-Induced Iron Deprivation. *J. Hepatol.* **2002**, *36* (1), 39−46.
(25) Farrugia, G.; Szurszewski, J. H. Carbon Monoxide, Hydrogen Sulfide, and Nitric Oxide as Signaling Molecules in the Gastrointestinal Tract. *Gastroenterology* **2014**, *147* (2), 303−313.
(26) Szabo, C.; Papapetropoulos, A. International Union of Basic and Clinical Pharmacology. CII: Pharmacological Modulation of H_2S Levels: H_2S Donors and H_2S Biosynthesis Inhibitors. *Pharmacol. Rev.* **2017**, *69* (4), 497−564.
(27) Joulia, E.; Metallo, C. M. Methionine and H_2S Alter Cancer-Immune Dialogue. *Nat. Metab.* **2023**, *5* (9), 1456−1458.
(28) Bonkovsky, H. L.; Troy, N.; McNeal, K.; Banner, B. F.; Sharma, A.; Obando, J.; Mehta, S.; Koff, R. S.; Liu, Q.; Hsieh, C. C. Iron and or Mutations as Comorbid Factors for Development and Progression of Chronic Hepatitis C. *J. Hepatol.* **2002**, *37* (6), 848−854.
(29) Choudhry, H.; Harris, A. L. Advances in Hypoxia-Inducible Factor Biology. *Cell Metab.* **2018**, *27* (2), 281−298.
(30) Saha, A.; Yadav, R.; Aldakov, D.; Reiss, P. Gallium Sulfide Quantum Dots with Zinc Sulfide and Alumina Shells Showing Efficient Deep Blue Emission. *Angew. Chem., Int. Ed.* **2023**, *62* (45), No. e202311317.
(31) Wang, J. J.; Sun, Z. L.; Wang, S. R.; Zhao, C. Y.; Xu, J. J.; Gao, S.; Yang, M.; Sheng, F. G.; Gao, S.; Hou, Y. L. Biodegradable Ferrous Sulfide-Based Nanocomposites for Tumor Theranostics through Specific Intratumoral Acidosis-Induced Metabolic Symbiosis Disruption. *J. Am. Chem. Soc.* **2022**, *144* (43), 19884−19895.
(32) La, P.; Ghiaccio, V.; Zhang, J. B.; Rivella, S. An Orchestrated Balance between Mitochondria Biogenesis, Iron-Sulfur Cluster Synthesis and Cellular Iron Acquisition. *Blood* **2018**, *132* (1), 1048.
(33) Nie, G. J.; Sheftel, A. D.; Kim, S. F.; Ponka, P. Overexpression of Mitochondrial Ferritin Causes Cytosolic Iron Starvation and Changes Cellular Iron Homeostatis. *Blood* **2004**, *104* (11), 3195.
(34) Spinelli, J. B.; Haigis, M. C. The Multifaceted Contributions of Mitochondria to Cellular Metabolism. *Nat. Cell Biol.* **2018**, *20* (7), 745−754.
(35) McArthur, K.; Whitehead, L. W.; Heddleston, J. M.; Li, L.; Padman, B. S.; Oorschot, V.; Geoghegan, N. D.; Chappaz, S.; Davidson, S.; Chin, H. S.; Lane, R. M.; Dramicanin, M.; Saunders, T. L.; Sugiana, C.; Lessene, R.; Osellame, L. D.; Chew, T. L.; Dewson, G.; Lazarou, M.; Ramm, G.; Lessene, G.; Ryan, M. T.; Rogers, K. L.; van Delft, M. F.; Kile, B. T. BAK/BAX Macropores Facilitate Mitochondrial Herniation and mtDNA Efflux during Apoptosis. *Science* **2018**, *359*, No. eaao6047.
(36) Nagata, S.; Tanaka, M. Programmed Cell Death and the Immune System. *Nat. Rev. Immunol.* **2017**, *17* (5), 333−340.
(37) Chen, Y. J.; Douglass, T.; Jeffes, E. W. B.; Xu, Q. C.; Williams, C. C.; Arpajirakul, N.; Delgado, C.; Kleinman, M.; Sanchez, R.; Dan, Q. H.; Kim, R. C.; Wepsic, H. T.; Jadus, M. R. Living T9 Glioma Cells Expressing Membrane Macrophage Colony-Stimulating Factor Produce Immediate Tumor Destruction by Polymorphonuclear Leukocytes and Macrophages via A "Paraptosis"-Induced Pathway that Promotes Systemic Immunity Against Intracranial T9 Gliomas. *Blood* **2002**, *100* (4), 1373−1380.
(38) Sperandio, S.; Poksay, K.; de Belle, I.; Lafuente, M. J.; Liu, B.; Nasir, J.; Bredesen, D. E. Paraptosis: Mediation by MAP Kinases and Inhibition by AIP-1/Alix. *Cell Death Differ.* **2004**, *11* (10), 1066−1075.
(39) Bruni, A.; Luciani, S. Effects of Atractyloside and Oligomycin on Magnesium-Stimulated Adenosine Triphosphatase and on Adenosine Triphosphate-Induced Contraction of Swollen Mitochondria. *Nature* **1962**, *196* (4854), 578−580.
(40) Grosse, L.; Wurm, C. A.; Brüser, C.; Neumann, D.; Jans, D. C.; Jakobs, S. Bax assembles into large ring-like structures remodeling the mitochondrial outer membrane in apoptosis. *Embo. J.* **2016**, *35* (4), 402−413.
(41) Balsa, E.; Soustek, M. S.; Thomas, A.; Cogliati, S.; García-Poyatos, C.; Martín-García, E.; Jedrychowski, M.; Gygi, S. P.; Enriquez, J. A.; Puigserver, P. ER and Nutrient Stress Promote Assembly of Respiratory Chain Supercomplexes through the PERK-eIF2α Axis. *Mol. Cell* **2019**, *74* (5), 877−890.E6.
(42) Lightfoot, A. P.; Morgan, R. S.; Cooper, R. G. Hmgb1 Induces Reactive Oxygen Species (Ros)-Dependent Activation of the Er Stress Pathway in C2c12 Myotubes. *Ann. Rheum. Dis.* **2016**, *75*, 521.1−521.
(43) Zhang, Y.-Y.; Han, Y.; Li, W.-N.; Xu, R.-H.; Ju, H.-Q. Tumor Iron Homeostasis and Immune Regulation. *Trends Pharmacol. Sci.* **2024**, *45* (2), 145−156.
(44) Zhou, T. X.; Xie, Y. J.; Hou, X. P.; Bai, W. W.; Li, X. Y.; Liu, Z. Y.; Man, Q.; Sun, J. Y.; Fu, D. Q.; Yan, J. R.; Zhang, Z. Y.; Wang, Y. F.; Wang, H. W.; Jiang, W. N.; Gao, S.; Zhao, T. S.; Chang, A. T.; Wang, X. C.; Sun, H. X.; Zhang, X. F.; Yang, S. Y.; Huang, C. B.; Hao, J. H.; Liu, J. Irbesartan Overcomes Gemcitabine Resistance in Pancreatic Cancer by Suppressing Stemness and Iron Metabolism via Inhibition of the Hippo/YAP1/c-Jun Axis. *J. Exp. Clin. Canc. Res.* **2023**, *42* (1), 111.
(45) Zhu, Z.; Shen, H. Y.; Xu, J. L.; Fang, Z.; Wo, G. Q.; Ma, Y.; Yang, K.; Wang, Y. L.; Yu, Q.; Tang, J. H. GATA3Mediates Doxorubicin Resistance by Inhibiting CYB5R2-Catalyzed Iron Reduction in Breast Cancer Cells. *Drug Resist. Update* **2023**, *69*, No. 100974.
(46) Shenoy, G.; Madhankumar, A.; Slagle-Webb, B.; Mrowczynski, O.; Schell, T.; Nesterova, D.; Lee, S.; Davalos, D.; Berens, M.; Lathia, J.; Barnholtz-Sloan, J.; Rubin, J.; Connor, J. ITMIC-31. Impact of Iron on Macrophage Immune Phenotype in the Glioblastoma Tumor Microenvironment. *Neuro-Oncology* **2019**, *21*, vi254.
(47) Taleb, M.; Maillet, I.; Le Bert, M.; Mura, C. Targeted Autophagy Disruption Reveals the Central Role of Macrophage Iron Metabolism in Systemic Iron Homeostasis. *Blood* **2022**, *140* (4), 374−387.
(48) Tan, X. L.; Ashby, T. C.; Zhu, Y. Q.; Li, C.; Shen, X. X.; Brockman, Q.; Gai, D. Z.; Johnson, S. K.; Yong, D.; Schinke, C. D.; Zangari, M.; van Rhee, F.; Shaughnessy, J.; Huang, D. M.; Frech, I.; Tricot, G. J.; Zhan, F. H. Iron Trafficking through Macrophages Regulates Signaling Pathways in Myeloma. *Blood* **2020**, *136* (1), 2.

https://doi.org/10.1021/acsnano.4c06199
ACS Nano XXXX, XXX, XXX−XXX